8

Strain Mediated Magnetoelectric Memory

N. Tiercelin[1], Y. Dusch[1], S. Giordano[1], A. Klimov[2], V. Preobrazhensky[3], and P. Pernod[1]

[1]*LIA LEMAC/LICS, IEMN UMR CNRS 8520, Univ. Lille, Centrale Lille, Lille, France*
[2]*Also with the Moscow Institute of Radio Engineering and Automation MIREA, Moscow, Russia; and V.A. Kotelnikov Institute of Radioengineering and Electronics, Moscow, Russia*
[3]*Also with A.M. Prokhorov General Physics Institute RAS, Moscow, Russia*

8.1 Introduction

As the need for energy efficient data processing and data storage booms, numerous efforts are made by research laboratories and industrials to develop the next generation of random access memories. In a 2013 report on emerging technologies to prepare for the post-CMOS era, the International Technology Roadmap for Semiconductors underlines the necessity to "Identify the most promising technical approach(es) to obtain electrically accessible, high-speed, high-density, low-power, (preferably) embeddable volatile and nonvolatile memories" [1]. In 2009, Mark Kryder and Chang Soo Kim compared the different existing approaches and technologies for the next generation [2]. They described the following solutions: ferroelectric random access memory (FRAM), magnetic memory (MRAM), spin torque transfer magnetic memory (STTRAM), phase change memory (PCRAM), carbon nanotube memory (NRAM), probe memories, holographic memory, conductive bridge memory (CBRAM), resistive memory (RRAM), racetrack memory, one electron memory (SEM), molecular memory and polymer memory. Among all these, the authors argued that only RRAM, CBRAM STTRAM and PCRAM seemed to be viable in the long run. The 2013 ITRS report confirmed this analysis and added carbon-based devices as well as Mott memories to the list of emerging technologies. Both studies are omitting the use of multiferroic materials, possessing coupled ferroelectric

Nanomagnetic and Spintronic Devices for Energy-Efficient Memory and Computing, First Edition.
Edited by Jayasimha Atulasimha and Supriyo Bandyopadhyay.

and ferromagnetic phases [3,4]. The interest in these materials is huge: using an electric field, one can write the information into the magnetic system with virtually "no energy," and read the information via magnetoresistive structures without destroying it. One of the most important reasons for considering multiferroic materials and structures comes from the global demand for low-power devices. In fact, it is generally accepted that the factor limiting the down-scaling and the high integration level in standard semiconductor electronics is power dissipation [5]. In order to circumvent this issue, a first step is the change of the physical state variable: the energy needed for switching the state of a bit in a standard electronic device is equal to at least $Nk_BT\ \ln(1/p)$ where N is the numbers of electrons (weakly or noninteracting carriers) involved in the process, k_B is the Boltzmann constant, T is the temperature and p is the bit error probability. On the other hand, if the information is encoded in the magnetization state of a monodomain ferromagnet composed of M strongly interacting spins, the switching process dissipates an energy equal to about $k_BT\ln(1/p)$, independently of the number M of spins [6]. Being able to control magnetization with an electric field would be the best way to reach the theoretical limits.

To date, very few materials with sufficient intrinsic multiferroic properties at room temperature were found suitable to be used in memory applications. The inclusion of multiferroic barriers into Magnetic Tuneling Junctions (MTJ) shows interesting results but still far below room temperature [7]. Another way is to amplify the effect of a room temperature multiferroic such as Cr_2O_3 using interfacial properties in order to control the value of an exchange field. This led to a magnetoelectric memory using electric field control and cooling through the Néel temperature [8,9]. Further studies led to an isothermal switching memory that still requires to be operated close to the Néel temperature @ 303 K [10]. Magnetoelectric effects can also be observed at the interface of magnetic materials and insulators thanks to the effect of the electric field on charge distribution [11,12]. This phenomenon involves very high electric fields and is limited to a few atomic layers at the interface.

On the other hand, a magnetoelectric effect can be obtained in composite structures that use strain-coupled piezoelectric and magnetostrictive materials that can operate at room temperature and offer several design possibilities [13,14]. A few recent works [15–19] related the effect of stress on the magnetic properties of magnetostrictive materials and some of the teams tried to use it as a memory device but could not achieve a simple switching procedure. In fact, due to symmetry concerns, the stress-mediated magnetoelectric effect unfortunately prevents electrically driven magnetization reversal, except when using so-called "ballistic" switching or using a magnetic field-assisted techniques. In both cases, the knowledge of the previous state of the memory element is needed to write a new bit, which dramatically complicates the writing process. Most of the proposed composite memory devices are thus toggle memories whose initial state must be known prior to writing operation [20] and may need precisely synchronized driving signals [21]. Other systems use the magnetocrystalline axes to obtain several equilibrium positions [22,23] but this requires the control of epitaxial growth.

In the present chapter the concept of a strain- or stress- mediated magnetoelectric memory cell with unequivocal (i.e., nontoggle) switching will be detailed. First, the concept of the memory will be presented as well as the switching procedure in the quasi-static case. The Landau-Lifshitz-Gilbert (LLG) equation will be solved in the case of a macro-spin model in order to assess the dynamic switching behavior of the magnetization. Then, the Eshelby formalism coupled with the Langevin approach will be used to study the influence of temperature on the stability and robustness of the memory.

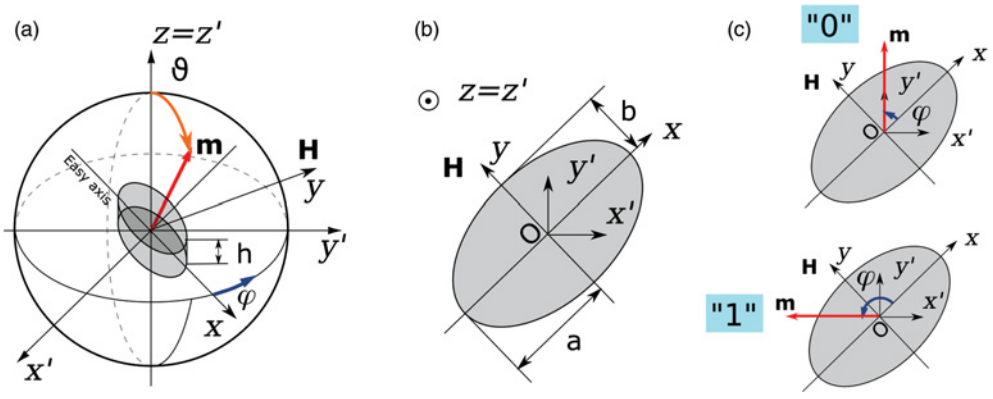

Figure 8.1 Geometry of the memory element

8.2 Concept of Unequivocal Strain- or Stress-Switched Nanomagnetic Memory

8.2.1 Magnetic Configuration and Equilibrium Positions

In order to break the symmetry, a solution is to apply a magnetic polarization on top of the uni-axial anisotropy. Figure 8.1 shows the configuration of a magnetoelastic elliptic cylinder lying on the xy plane. The x, y, x' and y' axes lie in the same plane, x' makes a $-\pi/4$ angle with respect to x. A static magnetic field H is applied in this plane, perpendicular to the easy axis of magnetization that lies along the x axis. In the case of a $TbFe_2$ (Terfenol) element, the magnetic parameters of the material are given in Table 8.1.

As a result of the competition between the external magnetic field and the shape and/or field-induced anisotropy (i.e., created by applying an external magnetic field during deposition), the

Table 8.1 Magnetic, magnetoelastic and elastic parameters of Terfenol used in simulations

Parameter	Symbol	Value
Magnetization (a)	M_s	64×10^4 A/m
First magneto-elastic coefficient (a,b)	λ_{111}	1.7×10^{-3}
Second magneto-elastic coefficient (a,b)	λ_{100}	0.1×10^{-3}
Effective magneto-elastic coefficient (c)	$\lambda_s = \frac{3}{5}\lambda_{111} + \frac{2}{5}\lambda_{100}$	1.06×10^{-3}
Young modulus of the particle (b)	E	110 GPa
Poisson ratio of the particle (b)	ν	0.35
Exchange stiffness constant (d)	A	10^{-11} J/m
Gilbert damping coefficient (e)	$\lvert\alpha\rvert$	0.3
Landé g-factor	g	2
Bohr magneton	$\mu_B = \frac{e\hbar}{2m_e}$	9.274×10^{-24} J T^{-1}
Gyromagnetic ratio	$\lvert\mathcal{G}\rvert = \frac{g\mu_B}{\hbar}$	1.76×10^{11} rad s^{-1} T^{-1}

(a) [24] (b) [25] (c) [26] (d) [27,28] (e) [29,30].

ellipsoidal element exhibits two stable equilibrium positions, which, unlike usual magnetic memory elements, are not directed along the easy axis of magnetization (EA). If no stress is applied, the magnetic free energy density can be written as

$$\tilde{w}_m = -\mu_0 M_s H \sin(\varphi)\sin(\vartheta) - \frac{1}{2}\mu_0 M_s H_{a,eq}\cos^2(\varphi)\sin^2(\vartheta), \tag{8.1}$$

where μ_0 is the vacuum permeability, M_s the saturation magnetization, H the external applied field, φ and ϑ are the angles of magnetization in spherical coordinates as specified on Figure 8.1(a) and (b), and $H_{a,eq}$ is the effective anisotropy field, which takes into account all the quadratic anisotropies, namely shape, magnetocrystalline and field induced magnetoelastic anisotropy. Higher-order anisotropies are neglected here. We first consider a disc-shaped element and henceforth suppose that magnetization remains in the (x, y) plane, that is, that $\sin(\vartheta) = 1$. Equation (8.1) simplifies into

$$\tilde{w}_m = -\mu_0 M_s H \sin(\varphi) - \frac{1}{2}\mu_0 M_s H_{a,eq}\cos^2(\varphi). \tag{8.2}$$

For $H < H_{a,eq}$, the equilibrium condition, $\partial\tilde{w}_m/\partial\varphi = 0$ gives $\varphi_0 = \arcsin(H/H_{a,eq})$. With $H = (\sqrt{2}/2)H_{a,eq}$, we obtain two distinct perpendicular equilibrium positions for $\varphi = 3\pi/4$ (arbitrarily named state "1") or $\varphi = \pi/4$ (state "0"), as illustrated in Figure 8.1(c).

Given the studied geometry and magnetic configuration, the energy barrier E_b is given as the difference of the free energy for $\varphi = \pi/2$ (lowest local energy maximum in the energy profile, see Figure 8.2) and $\varphi = \pi/4$ or $\varphi = 3\pi/4$ (symmetrical local energy minima). Therefore, with the volume πabh, $E_b = \pi abh[\tilde{w}_m(\varphi = \pi/2) - \tilde{w}_m(\varphi = \pi/4)]$.

With the condition $H = (\sqrt{2}/2)H_{a,eq}$, this expression leads to:

$$E_b = \frac{3 - 2\sqrt{2}}{4}\pi abh\mu_0 M_S H_{a,eq}. \tag{8.3}$$

For a structure allowing decent storage densities, such as the one described in Figure 8.6 with $a = 25\,\text{nm}$, $b = 15\,\text{nm}$, $h = 20\,\text{nm}$, and considering a saturation magnetization $M_s = 640\ \text{kA.m}^{-1}$, it is possible to induce a sufficient anisotropy to ensure a good stability of the stored information over time. For $H_{a,eq} \approx 300\,\text{kA.m}^{-1}$, $E_b \approx 60\,\text{k}_B\text{T}$. According to the Néel-Brown relaxation law [31,32], the error probability over a period t is given by $P = (1 - e^{-t/\tau})$ where $\tau = \tau_0 \exp(E_b/(k_B T))$. For typical values of $\tau_0 \approx 10^{-9}$ s this energy barrier is sufficient to ensure thermal stability over ten years at room temperature (293 K), making it usable for long-term data storage applications. A thorough discussion about the thermal stability will be led in Section 8.5.

Now that the existence of two stable positions is demonstrated, the question of the control of magnetization between these states arises. As explained in the following section, the application of uniaxial stress on the magnetostrictive material allows the deterministic selection of the final state, that is, without prior knowledge of the initial state.

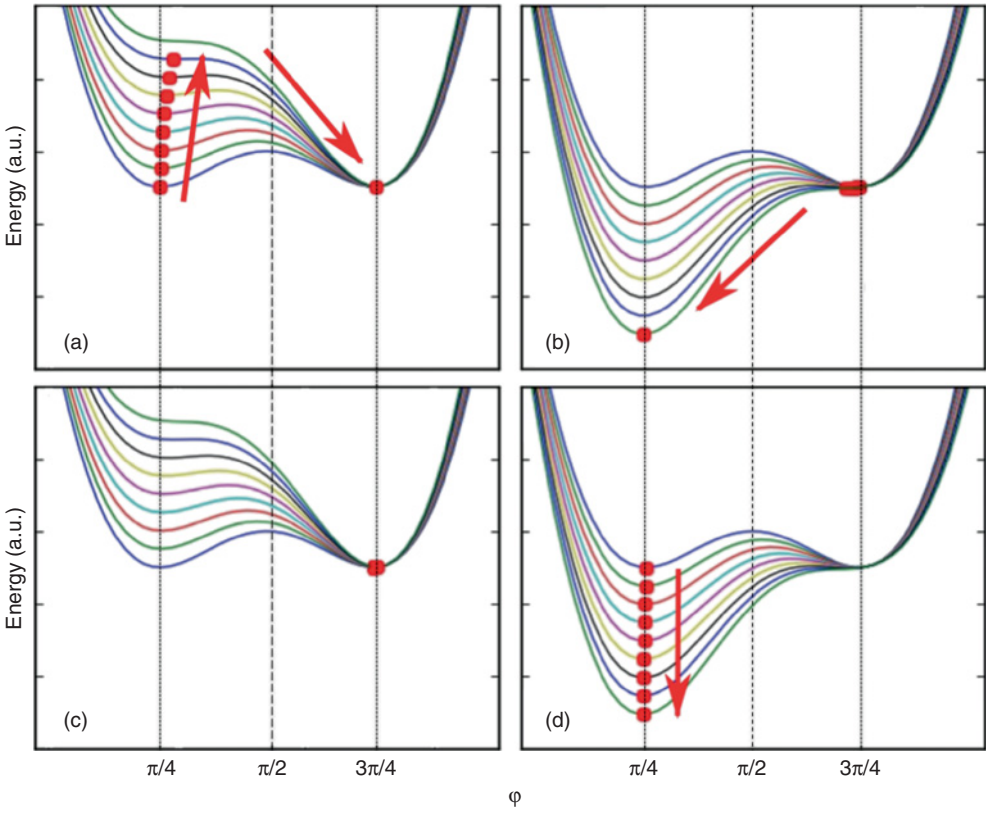

Figure 8.2 Quasi-static evolution of the free energy profiles and equilibrium positions of magnetization: (a) tensile stress, $\varphi_0 = \pi/4$; (b) compressive stress, $\varphi_0 = 3\pi/4$; (c) tensile stress, $\varphi_0 = 3\pi/4$; (d) compressive stress, $\varphi_0 = \pi/4$. Dots indicate the position of magnetization and arrows indicate the evolution of the equilibrium as the absolute value of stress increases.

8.2.2 Quasi-Static Stress-Mediated Switching

Let us assume that an in-plane stress σ_{ij} is applied to the magnetoelastic element, in the $\mathbf{x}'$,$\mathbf{y}'$, $\mathbf{z}'$ reference. The resulting magnetoelastic energy can be written as follows:

$$\tilde{w}_{me} = -\frac{3}{2}\lambda_S(\sigma_{x'x'} - \sigma_{y'y'})\cos^2\left(\varphi + \frac{\pi}{4}\right) - \frac{3}{2}\lambda_S\sigma_{x'y'}\cos\left(\varphi + \frac{\pi}{4}\right)\sin\left(\varphi + \frac{\pi}{4}\right). \tag{8.4}$$

For purely tensile/compressive stress, that is, $\sigma_{x'y'} = 0$, this quadratic expression shows that stress can be used to control the anisotropy and consequently to rotate magnetization.

A positive stress $\sigma = \sigma_{x'x'} - \sigma_{y'y'} > 0$ creates a magnetic easy axis along the $\mathbf{x}'$ axis whereas negative $\sigma < 0$ stress creates an easy plane of magnetization perpendicular to the $\mathbf{x}'$ axis. In the case of a piezoelectric or electrostrictive generation of stress, the stable position of magnetization can therefore be unequivocally controlled by voltage, depending on its sign. Using the same approach as introduced in recent literature [33], it is possible to numerically

simulate the quasi-static rotation of magnetization under extrinsic stress. At each iteration, the algorithm computes the local minimum of the free energy for $\sigma^{i+1} = \sigma^i + \delta\sigma$, starting from the previous equilibrium position at φ_0. Figure 8.2 shows the magnetic free energy profile of the particle as well as the equilibrium position of magnetization for compressive and tensile stresses and for different initial positions.

As shown in Figure 8.2, for a given initial state, the final state is an univocal function of the applied stress, when $|\sigma|$ reaches a critical value $|\sigma^{min}|$. This critical value is defined as the value for which the initial equilibrium position becomes unstable, that is, when $\partial^2(\tilde{w}_m + \tilde{w}_{me})/\partial\varphi^2 = 0$ and $\partial(\tilde{w}_m + \tilde{w}_{me})/\partial\varphi = 0$. In the example defined earlier, this value is numerically found to be $|\sigma^{min}| = 26.5$ MPa for both tensile and compressive stress. If we neglect the rotation of magnetization for $|\sigma| < |\sigma^{min}|$, a straightforward analysis shows that $|\sigma^{min}| \approx \mu_0 M_s H_{a,eq}/(6\lambda_s)$. This quasi-static approach is not sufficient to assess the capabilities of the system with regards to switching speed and dissipated power. The following section adresses these concerns through the use of the macrospin model and the Landau-Lifshitz-Gilbert (LLG) equation.

8.3 LLG Simulations – Macrospin Model

8.3.1 Landau-Lifshitz-Gilbert Equation and Effective Magnetic Field

Given the size of the magnetic particle, the strength of the exchange interaction for Terfenol and the anisotropy (see Table 8.1), the magnetic system is monodomain and all the spins behave collectively, as demonstrated through simulations using the open source micromagnetic software Magpar [34] with typical mesh cells sizes below 10 nm. The internal magnetization $\vec{M} = M_s\vec{\gamma}$ is then considered as uniform. M_s is its constant intensity and $\vec{\gamma}$ is a unit vector. Therefore, using the macrospin aproximation, the dynamic behavior of the memory element can also be investigated thanks to the well-known Landau-Lifshitz-Gilbert (LLG) equation [35–37]:

$$\frac{\mathrm{d}\vec{\gamma}}{\mathrm{d}t} = -\frac{\mathcal{G}}{M_s(1+\alpha^2)}\left[\vec{\gamma}\times\frac{\partial\tilde{w}}{\partial\vec{\gamma}} - \alpha\vec{\gamma}\times\left(\vec{\gamma}\times\frac{\partial\tilde{w}}{\partial\vec{\gamma}}\right)\right], \tag{8.5}$$

where $\mathcal{G}$ is the gyromagnetic ratio, α is the Gilbert damping parameter. Note that here, $\mathcal{G} < 0$ and $\alpha < 0$ to represent electrons precession.

The term $\frac{\partial\tilde{w}}{\partial\vec{\gamma}}$ is equivalent to an effective magnetic field $\vec{H}_{eff}$ taking into account the various interactions on the magnetization.

$$\vec{H}_{eff} = -\frac{1}{\mu_0 M_S}\frac{\partial\tilde{w}}{\partial\vec{\gamma}}, \tag{8.6}$$

$\vec{H}_{eff} = \vec{H} + \vec{H}_a + \vec{H}_d + \vec{H}_{me}$ with $\vec{H}$ being the contribution of the external field, $\vec{H}_a$ the uni-axial anisotropy, $\vec{H}_d$ the shape anisotropy, and $\vec{H}_{me}$ the magnetoelastic effects.

The demagnetizing field is given by $\vec{H}_d = -M_s\overline{\overline{\mathbf{N}}}\vec{\gamma}$, where $\overline{\overline{\mathbf{N}}} = (N_{ij})$ is the demagnetizing tensor depending on the geometry. In the case of the elliptical cylinder described in Figure 8.6 with parameters given in Table 8.2, the values of the components of the demagnetizing tensor

Table 8.2 Parameters used in simulations for the elliptic cylinder in a piezoelectric matrix (Figure 8.6)

Parameter	Symbol	Value
Axis along x	$2a$	50 nm
Axis along y	$2b$	30 nm
Height along z	h	20 nm
Distance between electrodes	d	130 nm
Electrode length	l_e	120 nm
Electrode height	h_e	50 nm
PZT relative dielectric constant	ε_r	3000
Approximate Capacitance	$C = l_e h_e \varepsilon / d$	1.22 fF

can be calculated [38] and in our case, $N_{xx} \approx 0.2$, $N_{yy} \approx 0.35$ and $N_{zz} \approx 0.45$. Assuming uniaxial stress, the following expression can therefore be obtained in basis $(\mathbf{x}, \mathbf{y}, \mathbf{z})$:

$$\vec{H}_{eff} = \left(\frac{1}{2} H_a \gamma_x - M_s N_{xx} \gamma_x + \frac{3\lambda_s \sigma}{2\mu_0 M_s} (\gamma_x - \gamma_y), \right.$$
$$H - \frac{1}{2} H_a \gamma_y - M_s N_{yy} \gamma_y - \frac{3\lambda_s \sigma}{2\mu_0 M_s} (\gamma_x - \gamma_y),$$
$$\left. -M_s N_{zz} \gamma_z \right). \tag{8.7}$$

8.3.2 Memory Parameters

The parameters used for the magnetoelastic particle are presented in Table 8.1. As it is supposed amorphous, its effective magnetostriction coefficient can be evaluated using λ_{111} and λ_{100} through the following formula [26]:

$$\lambda_s = \frac{3}{5} \lambda_{111} + \frac{2}{5} \lambda_{100} \approx 1.06 \times 10^{-3} \tag{8.8}$$

We assumed a damping coefficient equal to $\alpha = 0.3$ which is a reasonable value for ferrimagnetic Rare Earth-Transition Metal (RE-TM) alloys, and a gyromagnetic ratio $\mathcal{G} = g\mu_B/\hbar \approx 1.76 \times 10^{11}$ rad.s^{-1}.T^{-1} with $g = 2$ the Lande factor of the electron and μ_B the Bohr magneton.

The geometry parameters used for the simulations are given in Table 8.2. The external magnetic field was chosen equal to $H = 150$ kA.m^{-1}. Taking into account the shape anisotropy, the additional field-induced anisotropy is chosen equal to $H_a = 93\ 750$ A.m^{-1}, so that the equilibrium positions are perpendicular. Such an anisotropy can be obtained in nanostructured magnetostrictive thin films, as demonstrated in [39] or [40]. In this model, we assume that stress reaches instantly its set-point value and remains constant hereafter. Nonetheless, as illustrated in [20], more complex schemes can be envisioned and studied, in particular in the case of adiabatic charge of a piezoeletric capacitor.

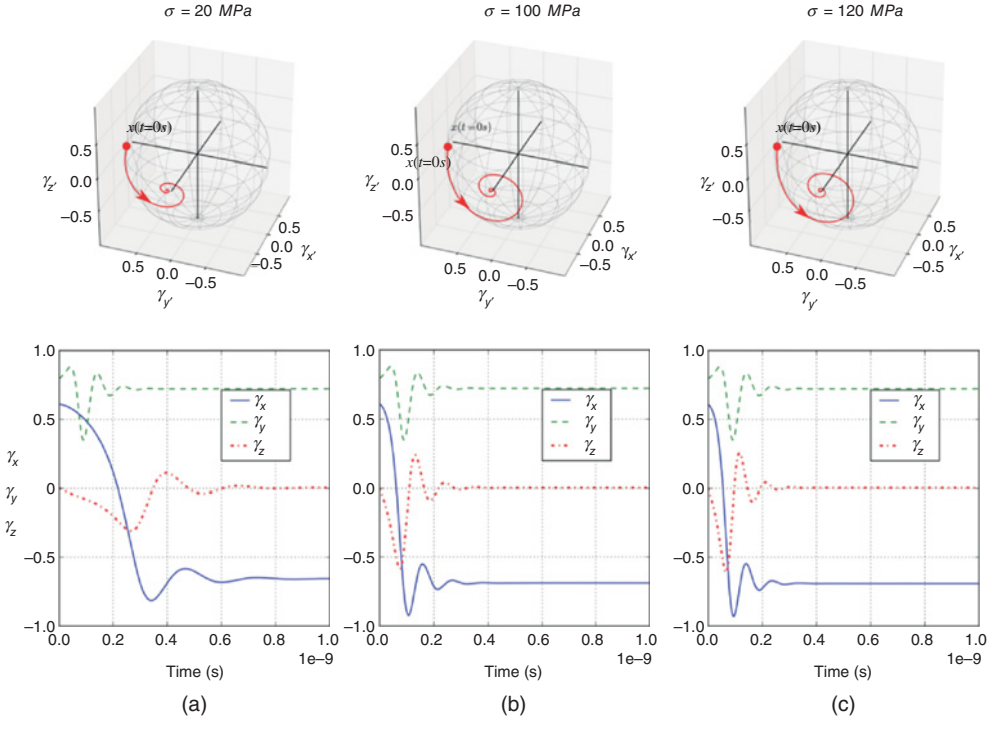

Figure 8.3 Trajectories of magnetization $\vec{\gamma}$ from state "0" for $\sigma = 20\,MPa$ (a), $\sigma = 100\,MPa$ (b) and $\sigma = 120\,MPa$ (c). Top: in the $\mathbf{x}'$, $\mathbf{y}'$, $\mathbf{z}'$ reference; Bottom: $\vec{\gamma}$ components in the $\mathbf{x}$, $\mathbf{y}$, $\mathbf{z}$ reference.

8.3.3 Results of the Macrospin Model

8.3.3.1 Trajectories

Equation 8.5 can be solved for various stress values using a standard numerical routine [41]. The initial positions of magnetization are determined by preliminary simulations.

Figure 8.3 and 8.4 present the trajectories and the temporal evolution of $\vec{\gamma}$ for tensile (Figure 8.3) and compressive (Figure 8.4) stress along $\mathbf{x}'$. For tensile stress, the trajectories of $\vec{\gamma}$ remain similar, irrespective of the value of $|\sigma|$ is. The vector $\vec{\gamma}$ leaves its initial equilibrium position before precessing around the new stable position defined by the magnetoelastically induced easy axis. In the case of compressive stress, the behavior of $\vec{\gamma}$ changes dramatically. For values of $|\sigma|$ ranging approximately from 7 to 100 MPa, magnetization dynamics exhibit the same behavior as in the previous case. For very high values of stress (>110 MPa), the ringing phenomenon occurs around both the initial equilibrium position and the final equilibrium position. An intermediate case, in which $\vec{\gamma}$ reaches a wrong equilibrium position can also be observed, as shown on Figure 8.4(b). Nonetheless, numerical simulations show that when stress is removed, magnetization reaches the correct desired position. These discrepancies originate from the nature of the magnetoelastic anisotropy. In the case of tensile stress, magnetoelastic coupling creates an easy axis of magnetization whereas compressive stress creates an easy plane of magnetization. In any case, deterministic switching can occur.

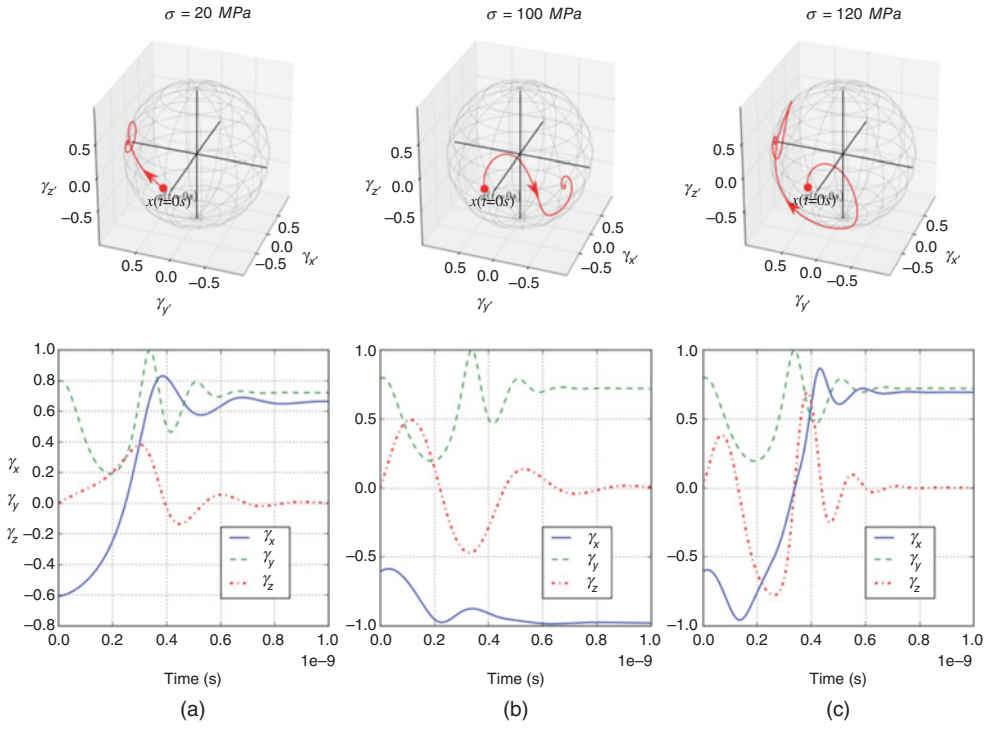

Figure 8.4 Trajectories of magnetization $\vec{\gamma}$ from state "1" for $\sigma = -20\,MPa$ (a), $\sigma = -100\,MPa$ (b) and $\sigma = -120\,MPa$ (c). Top: in the $\mathbf{x}'$, $\mathbf{y}'$, $\mathbf{z}'$ reference; Bottom: $\vec{\gamma}$ components in the $\mathbf{x}$, $\mathbf{y}$, $\mathbf{z}$ reference.

It can be noted that even if simulation have been performed for very large stress values, the minimal stress required to induce switching has been numerically evaluated to $|\sigma^{min}| \approx 7$ MPa in both tensile and compressive case. For practical applications, the values of required stress will remain in the 20 MPa range. Let us also note here that a lower energy barrier leads to a decrease of the minimal stress, at the expense of retention time.

8.3.3.2 Switching Time

The switching time $t_{1\%}$ of the system is defined as the time by which $\gamma_{y'}$ is comprised between 0.99 and 1.01 times its equilibrium value. This choice for $t_{1\%}$ is arbitrary and does not account for the maximum clock frequency of the system, but only stands for an image of the time needed to reach the equilibrium under extrinsic stress. Figure 8.5 presents the value of $t_{1\%}$ as a function of the modulus of the applied stress for tensile and compressive stress.

In any case, for values of stress above $|\sigma| \approx 15$ MPa, switching time can be made inferior to 0.5 ns, thus allowing at least clock frequencies up to around 1 GHz.

8.3.3.3 Dissipated Energy

Let us now consider the embedding of a magnetostrictive element in a Lead-Zirconate-Titanium (PZT) piezoelectric matrix, as illustrated on Figure 8.6. As shown in [42], such a configuration allows the generation of uniaxial stress in the magnetostrictive element.

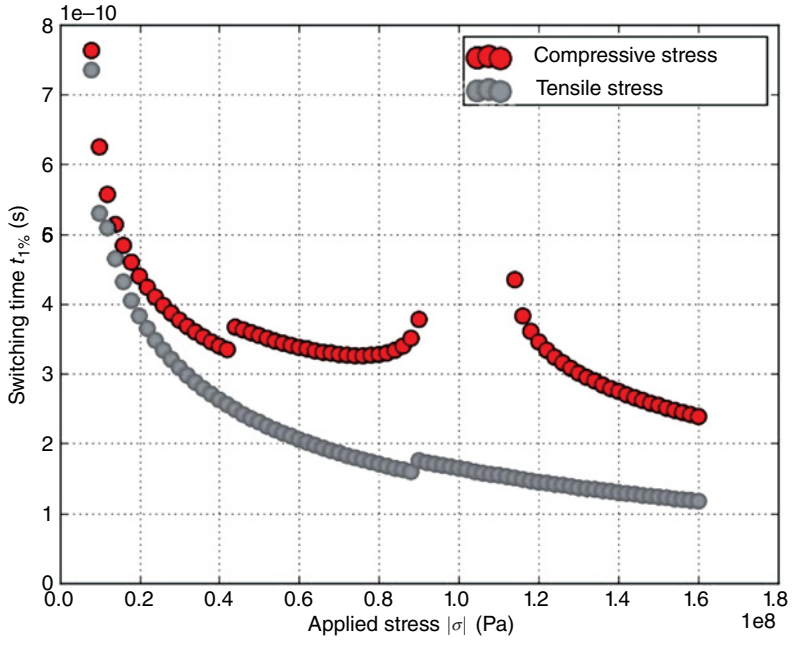

Figure 8.5 Switching time $t_{1\%}$ as a function of the modulus of the applied stress $|\sigma|$. Discontinuities around 42 MPa and 90 MPa are calculation artifacts due to the definition of the switching time.

While considering the dynamic switching of the memory element, it is necessary to consider the energy dissipation inside the PZT element regarded as a capacitor. Indeed, each set or reset cycle is composed of nonadiabatic charge and discharge of the capacitor and therefore dissipates an amount of energy equal to $E_{d,e} = CV^2$. From an electrical point of view, the system can be considered in first approximation as a parallel plate capacitor. Hence, $C \approx \varepsilon S/d$, where $\varepsilon = \varepsilon_r \varepsilon_0$ is the dielectric constant of PZT, S is the surface of the electrodes and d the distance between them. With the geometric parameters specified in Figure 8.6 and Table 8.2, we find $C \approx 1.22$ fF. With $V = 0.4$ V, we find $E_{d,e} = CV^2 \approx 0.2$ fJ. Please note that the capacitance

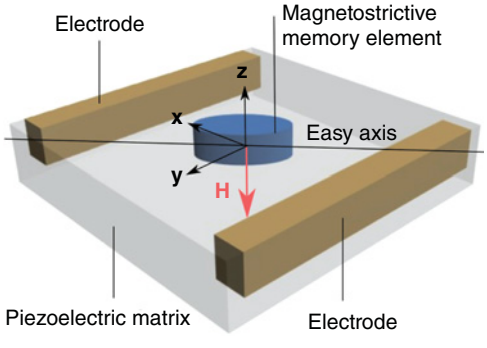

Figure 8.6 Geometry of the piezoelectric matrix.

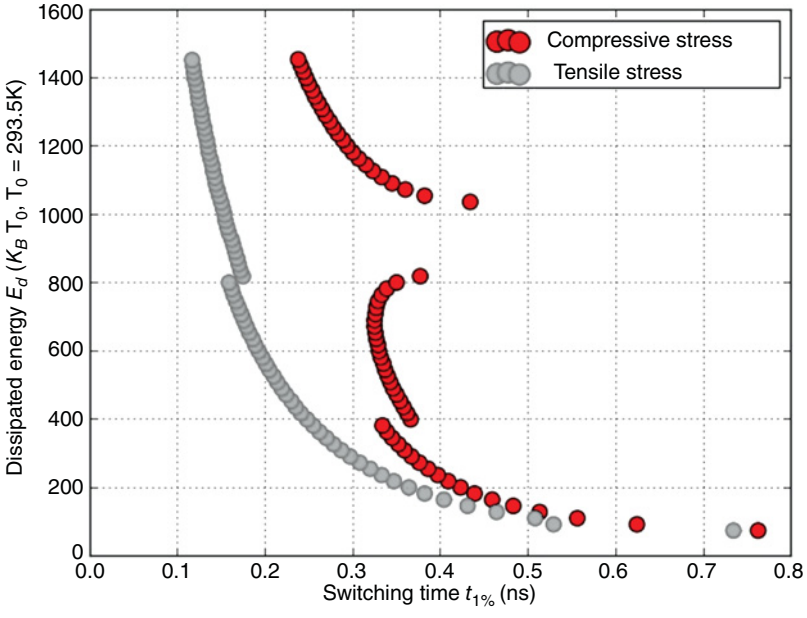

Figure 8.7 Dissipated magnetic energy versus switching time.

of the interconnections is not taken into account here. Compared to CMOS based devices, the advantage of the magnetoelectric system is that only low voltages are required to induce switching, thanks to coupled high magnetostrictive and piezoelectric coefficients.

The other source of dissipation lies in the precession of magnetization and its interactions with the surrounding lattice. The energy dissipated during the precession of magnetization can be evaluated by the following expression [43]:

$$E_{d,m} = -\int_0^{\infty} \frac{v d\tilde{\omega}}{dt} dt = v\frac{\alpha M_s}{\mathcal{G}} \int_0^{\infty} \left(\frac{d\vec{\gamma}}{dt}\right)^2 dt. \tag{8.9}$$

with v being the volume of the magnetic element. This dissipated energy has been computed for different values of stress and, as expected, this energy decreases as the switching time increases, as illustrated in Figure 8.7.

For σ up to 100 MPa, which corresponds to voltages lower than 0.4 V as shown in [42], the total energetic writing cost is inferior to $E_d = E_{d,m} + E_{d,e} \approx 0.21$ fJ/bit. Compared to other switching methods, this energy is still 3 orders of magnitude below [2].

8.4 LLG Simulations – Eshelby Approach

We present in this section a different methodology introduced to obtain a simple model, able to take into account all the coupling phenomena through a single energy function for the

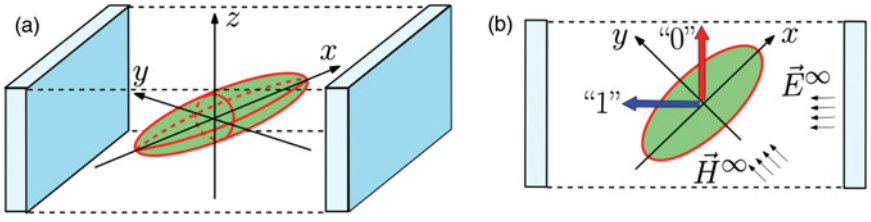

Figure 8.8 Magnetoelastic particle inserted between two electrodes in a piezoelectric matrix: three-dimensional scheme (a) and top view (b). The easy axis and the hard axis of the particle are along the x and y axis, respectively. The electrodes generate the electric field $\vec{E}^{\infty}$ at $\varphi = 3\pi/4$ while the magnetic field $\vec{H}^{\infty}$ is applied at $\varphi = \pi/2$. *Source*: Giordano *et al*., 2013b [48]. Reproduced by permission of IOP Publishing.

particle. So doing, this energy function can easily be coupled with the LLG equation (see Equation (8.5)) in order to analyze the dynamics of the system. To do this, we introduce the hypothesis of an ellipsoidal magnetoelastic particle embedded in a piezoelectric matrix (see Figure 8.8). This assumption on the geometry allows us to exploit the Eshelby theory, applied to the fully coupled magneto-electro-elastic case. As a matter of fact, it is well known that an elastic ellispoidal particle embedded in a different matrix, when subjected to a remotely applied mechanical load, exhibits uniform stress and strain inside it [44]. The uniformity of the physical fields is also confirmed to the general case with a linear magneto-electro-elastic coupling [45–47] and is relevant to our memory structure. As previously discussed in this chapter, we elaborate the energy function by considering the Zeeman term, the magnetic anisotropy and the magnetostriction. By analysing the coupling with the external magnetic and electric fields, we provide a general form for the energy function that is able to describe the magnetostriction orientation in terms of the applied fields and is useful for studying the static and dynamic behaviors of the memory.

8.4.1 Geometry of the Memory Element

We consider a magnetoelastic ellipsoidal particle embedded in a piezoelectric matrix (see Figure 8.8 for details) and we briefly introduce the formalism developed for modeling its behavior. As earlier, the polarizing field $\vec{H}^{\infty}$ is applied along the y axis in order to define the two equilibrium positions "1" and "0." A more general case is described by this model since we do not consider the applied stress but the electric field $\vec{E}^{\infty}$ created upon application of a voltage across the electrodes. The piezoelectric matrix is used to change the state of the memory: depending on its sign, the electric field $\vec{E}^{\infty}$ induces a tension or a compression along the direction perpendicular to the planes of the parallel electrodes. Again, a tensile stress stores the bit "1" while a compressive stress stores "0."

As a typical example, we adopt a nanoparticle made of $TbFe_2$ (Terfenol) with semi-axes a_1, a_2, and a_3 inserted in a Lead Zirconate Titanate (PZT-5H) matrix. The internal magnetization $\vec{M} = M_s\vec{\gamma}$ is uniform (M_s is its constant intensity and $\vec{\gamma}$ is a unit vector) because of the small

Table 8.3 Parameters used in simulations for the elliptic cylinder in a piezoelectric matrix (Figure 8.5)

Parameter	Symbol	Value
Axis along x	$2a_1$	45 nm
Axis along y	$2a_2$	25 nm
Axis along z	$2a_3$	20 nm
Electrode length	l_e	70 nm
Electrode height	h_e	20 nm
PZT relative dielectric constant	ε_r	3000
Approximate capacitance	$C = l_e h_e \varepsilon / d$	0.3 fF

size of the particle. The direction $\vec{\gamma}$ can be determined by minimizing the following energy function [49]

$$w(\vec{\gamma}) = -\mu_0 M_s \vec{\gamma} \cdot \vec{H} + \varphi_a(\vec{\gamma}) - \hat{T} : \hat{\varepsilon}_\mu(\vec{\gamma}). \tag{8.10}$$

The first term (Zeemann energy) describes the effect of the local magnetic field $\vec{H}$. The second term $\varphi_a(\vec{\gamma})$ represents the anisotropic energy [42]. In our case we assume the usual uniaxial form $\varphi_a(\vec{\gamma}) = -(1/2)\mu_0 M_s H_a \gamma_x^2$. Finally, the third term represents the elastic and magnetoelastic energy, where $\hat{T}$ is the local stress and $\hat{\varepsilon}_\mu(\vec{\gamma})$ is the strain describing the magnetostriction. We use the standard expression $\hat{\varepsilon}_\mu(\vec{\gamma}) = (\lambda_s/2)(3\vec{\gamma} \otimes \vec{\gamma} - \hat{I})$ where $\hat{I}$ is the identity tensor and the effective magnetostriction coefficient λ_s can be evaluated as in Table 8.1 where one can find the main parameters of Terfenol. Similarly, in Table 8.3 one can find the main parameters of the system.

To conclude, we summarize the constitutive equations of the particle: the magnetic behavior is governed by $\vec{B} = \mu_0[\vec{H} + M_s\vec{\gamma}]$ where $\vec{B}$ is the magnetic induction and the elastic one by $\hat{T} = \hat{L}_2\{\hat{\varepsilon}_0 - \hat{\varepsilon}_\mu(\vec{\gamma})\}$ where $\hat{\varepsilon}_0$ is the local strain tensor (referred to the demagnetized particle) and $\hat{L}_2$ is the stiffness tensor of the particle. Here $\vec{\gamma} = \vec{\gamma}(\vec{H}, \hat{T})$ can be found through the nonlinear minimization of Equation (8.10).

8.4.2 Coupling with the External Magnetic Field

It is important to know the relationship between the local magnetic field $\vec{H}$ and the externally applied magnetic field $\vec{H}^\infty$. As recently discussed [50], the solution of this problem is given by

$$\begin{aligned} \vec{H} &= [\hat{I} - \hat{S}_m(\hat{I} - \hat{\mu}_1^{-1}\mu_0)]^{-1}\left[\vec{H}^\infty - \hat{S}_m\hat{\mu}_1^{-1}\mu_0 M_s\vec{\gamma}\right] \\ &= \hat{A}\vec{H}^\infty + \hat{N}\vec{\gamma}, \end{aligned} \tag{8.11}$$

where the tensor $\hat{S}_m$ is the magnetic Eshelby tensor [51, 52], μ_0 is the vacuum magnetic permeability and $\hat{\mu}_1$ is the magnetic permeability tensor of the piezoelectric matrix. Tensors $\hat{A}$ and $\hat{N}$ can be directly identified by the first line of Equation (8.11). The local magnetic field is therefore explicitly written in terms of the remotely applied magnetic field and of the internal magnetization orientation.

8.4.3 Coupling with the External Electric Field and Elastic Stress

The coupling with the external electric and elastic fields is mediated by the piezoelectric matrix, representing the environment where the particle is inserted. We search for the relationship between the local stress $\hat{T}$ and the applied electric field $\vec{E}^{\infty}$ and the remote elastic strain $\hat{\varepsilon}^{\infty}$. We remember that the constitutive equation of the matrix can be written as $\hat{T} = \hat{L}_1\hat{\varepsilon} + \hat{Q}_1\vec{E}$ and $\vec{D} = \hat{R}_1\hat{\varepsilon} + \hat{\varepsilon}_1\vec{E}$ where $\hat{L}_1$ is the elastic stiffness tensor, $\hat{\varepsilon}_1$ is the permittivity tensor and $\hat{Q}_1$ and $\hat{R}_1 = -\hat{Q}_1^T$ are the piezoelectric tensors of the matrix. The tensor properties of the PZT-5H matrix can be found in literature [53]. The magnetoelastic particle is inserted into the piezoelectric matrix with a specific initial magnetization direction $\vec{\gamma}_0$ and a corresponding magnetostriction $\hat{\varepsilon}_\mu(\vec{\gamma}_0)$. We measure the local strain (within the particle) with respect to such an initial state and we therefore define $\hat{\varepsilon} = \hat{\varepsilon}_0 - \hat{\varepsilon}_\mu(\vec{\gamma}_0)$. Here, $\hat{\varepsilon}_0$ is the local strain tensor referred to the demagnetized particle. Practically, we observe that $\vec{\gamma}_0$ is aligned with the x-axis and therefore $\vec{\gamma}_0 = \pm\vec{e}_1$ (where $\vec{e}_i$ is the unit vector along the i-th axis). Hence, the constitutive equations of the particle in the new reference frame read $\hat{T} = \hat{L}_2\{\hat{\varepsilon} - [\hat{\varepsilon}_\mu(\vec{\gamma}) - \hat{\varepsilon}_\mu(\vec{\gamma}_0)]\}$ and $\vec{D} = \hat{\varepsilon}_2\vec{E}$ where $\hat{L}_2$ and $\hat{\varepsilon}_2$ are the elastic stiffness and the permittivity tensor of the particle, respectively.

The coupling problem can be approached and solved by means of the multiphysics Eshelby formalism [44, 50, 54, 55]. The local stress depends on the external electric field, the external elastic stress and on the magnetization direction. In fact, we proved the explicit relation

$$\hat{T} = \hat{C}\hat{\varepsilon}^{\infty} + \hat{D}\vec{E}^{\infty} + \hat{F}[\hat{\varepsilon}_\mu(\vec{\gamma}) - \hat{\varepsilon}_\mu(\vec{\gamma}_0)], \tag{8.12}$$

where the tensors $\hat{C}$, $\hat{D}$ and $\hat{F}$ can be calculated through the refined procedures described in literature [50]. They depend on the physical properties of the two phases and on the piezoelectric Eshelby tensor [45–47].

8.4.4 Static Behavior of the System

We can now combine previous results in order to obtain a generalized energy function describing the static behavior of the memory system. The set of equations describing the system is constituted of the energy minimization, Equation (8.10), the coupling with the external magnetic field $\vec{H} = \vec{H}(\vec{H}^{\infty}, \vec{\gamma})$, Equation (8.11), and the coupling with the external electric and elastic fields $\hat{T} = \hat{T}(\hat{\varepsilon}^{\infty}, \vec{E}^{\infty}, \vec{\gamma})$, Equation (8.12). This problem corresponds to the minimization of a new energy function defined as

$$\begin{aligned}\tilde{w} = &-\mu_0 M_s\vec{\gamma}\cdot\hat{A}\vec{H}^{\infty} - \frac{1}{2}\mu_0 M_s\vec{\gamma}\cdot\hat{N}\vec{\gamma} + \varphi_a(\vec{\gamma})\\ &-\hat{C}\hat{\varepsilon}^{\infty} : \hat{\varepsilon}_\mu(\vec{\gamma}) - \hat{D}\vec{E}^{\infty} : \hat{\varepsilon}_\mu(\vec{\gamma})\\ &-\frac{1}{2}\hat{F}\hat{\varepsilon}_\mu(\vec{\gamma}) : \hat{\varepsilon}_\mu(\vec{\gamma}) + \hat{F}\hat{\varepsilon}_\mu(\vec{\gamma}_0) : \hat{\varepsilon}_\mu(\vec{\gamma}).\end{aligned} \tag{8.13}$$

Such an expression provides the final magnetization orientation in terms of the external fields applied to the structure. This procedure assumes a quite perfect particle-matrix interface. Nevertheless, we remember that nanostructures bahavior is deeply affected by interface defects occurring at the boundary between different phases [56–58]. We can directly apply Equation

(8.13) to investigate the behavior of the memory element by letting $\hat{\varepsilon}^{\infty} = 0$, $\vec{H}^{\infty}$ along the y-axis and $\vec{E}^{\infty}$ along the direction identified by $\varphi = \pi/4$, $\vartheta = 0$ (where φ and ϑ are the standard spherical coordinates). As an example, calculations are led using the parameters summarized in Table 8.3. The effective anisotropic field H_a of the magnetoelastic element is set at 18×10^4 A/m, whereas the external magnetic field H^{∞} is 50×10^4 A/m. When $\vec{E}^{\infty} = 0$ we observe two equivalent stable positions around $\varphi = \pi/4$, $\vartheta = 0$ and $\varphi = 3\pi/4$, $\vartheta = 0$ corresponding to the arrows in Figure 8.8. This is shown in Figure 8.9(b) where $\tilde{w}$ is represented through a polar plot (in terms of φ and ϑ). The solid curve corresponds to $\vartheta = 0$ and shows two minima (points A and B). In Figure 8.9(a) we have an applied compressive stress (V = +0.5 V and $\vec{E}^{\infty} = -3.85 \times 10^6$ V/m) generating a single minimum point A (bit "0"). Conversely, in Figure 8.9(c) we have an applied tensile stress ($V = -0.5$ V and $\vec{E}^{\infty} = +3.85 \times 10^6$ V/m) corresponding to the minimum point B (bit "1"). This behavior is consistent with the quasi-static evolution of the magnetoelastic particle submitted to stress that was descibed in Section 8.2.2. It is again evident that the form of the energy function allows us to obtain a non-toggle switching scheme for the memory element.

8.4.5 Dynamic Behavior of the System

As already explained in Section 8.3, the magnetic system is assumed to be monodomain and the dynamics of the magnetization are described by the LLG equation (see Equation (8.5)). The results of the integration of this equation are shown in Figure 8.10 for two different values of the applied voltage: ±0.3 V (which means $E^{\infty} = \pm 2.3 \cdot 10^6$ V/m) and ±0.5 V (which means $E^{\infty} = \pm 3.85 \cdot 10^6$ V/m). A complete cycle with the two switching phases is represented and reveals two important properties: (i) the transition times are always in the sub-nanosecond scale (<0.4 ns) and (ii) such times decrease with larger applied voltages (in a given range, see later). As already seen in Section 8.3, and while in the static analysis of the system we have described the commutation strategy on the plane, the actual dynamic case is more complex. The general behavior is the result of the interplay between the in-plane and the out-of-plane motion of $\overrightarrow{\gamma(t)}$. This point becomes evident by the observation of the component γ_z in Figure 8.10(b).

In Figure 8.10(c) we can also find the behavior of the local stress during the complete cycle. We have defined the quantities $T_{\vec{n}} = \vec{n} \cdot \hat{T}\vec{n}$ and $T_{\vec{m}} = \vec{m} \cdot \hat{T}\vec{m}$ where $\vec{n} = (\sqrt{2}/2, \sqrt{2}/2, 0)$ and $\vec{m} = (-\sqrt{2}/2, \sqrt{2}/2, 0)$. They represent the specific force [N/m^2] along the directions at $\varphi = \pi/4$ and $\varphi = 3\pi/4$, respectively. We remark that when these quantities are positive we have a traction and when they are negative a compression. In the phase D (writing of the bit "1") we find a traction along $\vec{m}$ ($T_{\vec{m}} \simeq 90$ MPa with -0.5 V and $T_{\vec{m}} \simeq 55$ MPa with -0.3 V) induced by the positive electric field applied to the piezoelectric matrix. Conversely, in the phase C (writing of the bit "0") a compression along $\vec{m}$ ($T_{\vec{m}} \simeq -60$ MPa with +0.5 V and $T_{\vec{m}} \simeq -20$ MPa with +0.3 V) is generated by the negative electric field. It is important to observe that the stable points A and B are characterized by a nonzero state of stress since the tractions or compressions are absent only when the magnetization is oriented along the x-axis (in both directions). Therefore, the state of stress in A and B is maintained at the levels indicated in Figure 8.10(c) by the magnetic field $\vec{H}^{\infty}$. Interestingly enough, we observe that the values of $T_{\vec{n}}$ and $T_{\vec{m}}$ are inverted passing from point A to point B because of the symmetry of

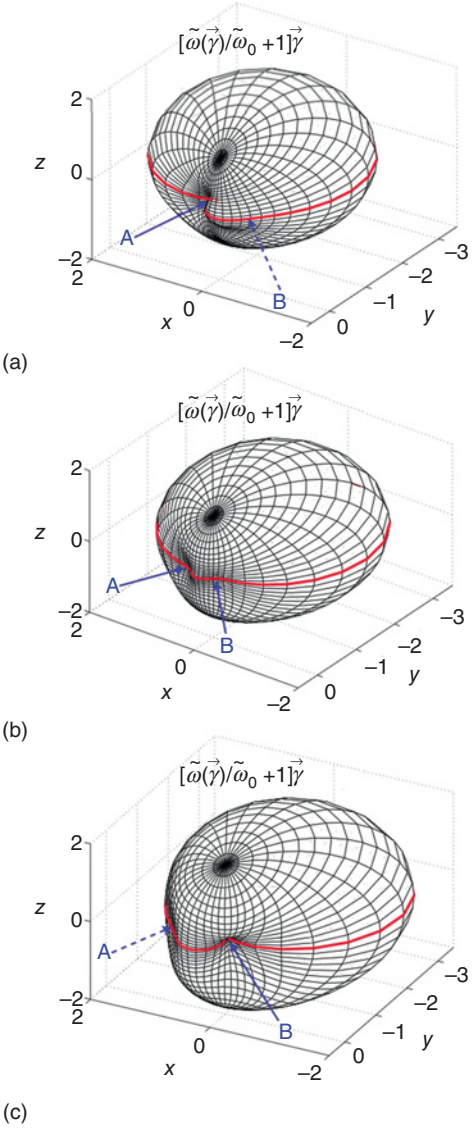

Figure 8.9 Representation of $\tilde{w}(\vec{\gamma})$ [J/m^3] through polar plots for different values of the applied voltage: (a) $V = +0.5$ V or $E^{\infty} = -3.85 \times 10^6$ V/m (compression), (b) $V = 0$ V, and (c) $V = -0.5$ V or $E^{\infty} = +3.85 \times 10^6$ V/m (traction). The solid curve corresponds to $\vartheta = 0$ and shows the positions of points A and B for the three different cases. We used $\tilde{w}_0 = 2.7 \times 10^5$ J/m^3 for obtaining $\tilde{w}(\vec{\gamma}) + \tilde{w}_0 > 0$ for any direction $\vec{\gamma}$.

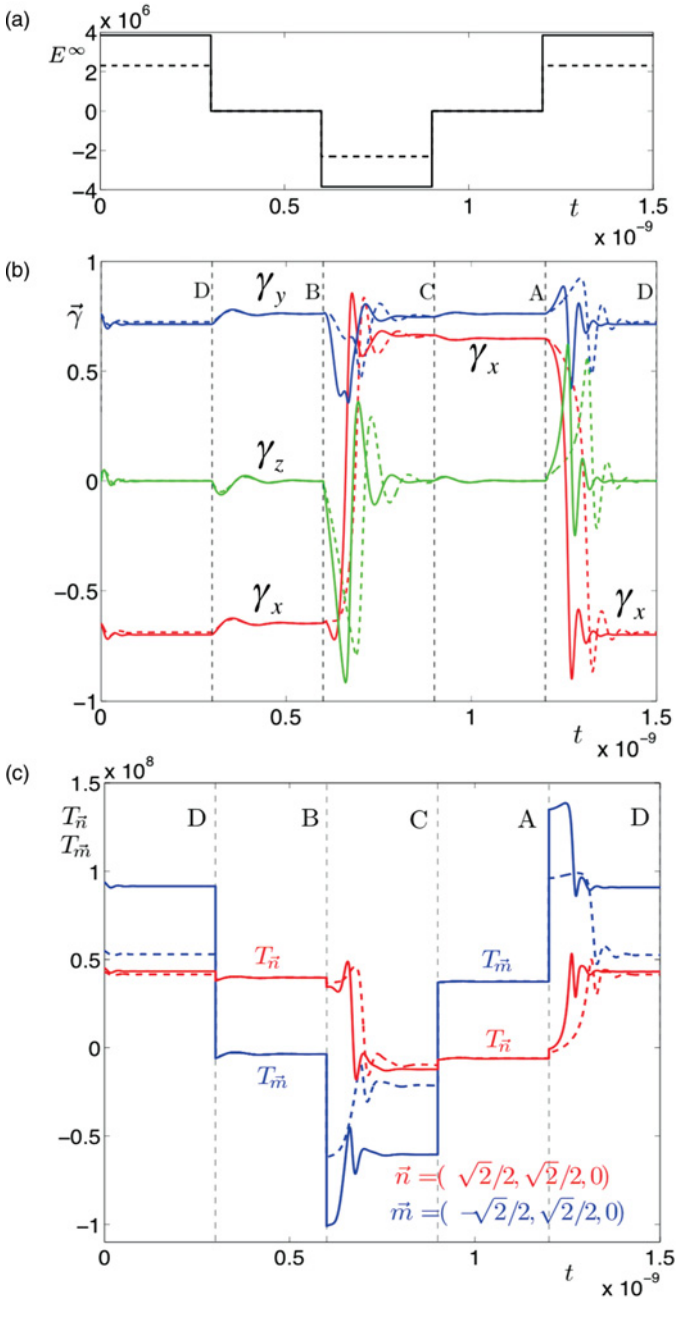

Figure 8.10 (a) Time behavior of the imposed electric field E^{∞} [V/m] and (b) the corresponding evolution of the magnetization direction $\vec{\gamma}$ for a voltage equals to ± 0.5 V (solid lines) and ± 0.3 V (dashed lines). (c) Dynamic behavior of the local stress [N/m^2]. The tractions $T_{\vec{n}} = \vec{n} \cdot \hat{T}\vec{n}$ and $T_{\vec{m}} = \vec{m} \cdot \hat{T}\vec{m}$ along the directions $\vec{n} = (\sqrt{2}/2, \sqrt{2}/2, 0)$ and $\vec{m} = (-\sqrt{2}/2, \sqrt{2}/2, 0)$ are shown. *Source*: Giordano *et al.*, 2012 [50]. Reproduced with permission of the American Physical Society.

the system. Nevertheless, such a geometrical symmetry does not lead to the same dynamical features of the switching phases B–C and A–D. In fact, the phase B–C is characterized by a compression inducing a *planar anisotropy* from the magnetic point of view (on the plane perpendicular to $\vec{m}$). On the other hand, the phase A–D is characterized by inducing an *axial anisotropy* for the magnetization (along the direction $\vec{m}$).

In particular, the differences between the physical phenomena involved in phases B–C and A–D are reflected in the switching times as reported in Figure 8.11. We consider the magnetization direction $\vec{\gamma} = (\gamma_x, \gamma_y, \gamma_z)$ and the scalar quantity $G = \gamma_x + \gamma_y + \gamma_z$ as functions of the time during the commutation phases. We define the switching time as the first instant of time t_m (of the commutation phase) satisfying the condition $G(t) - G(\infty) < \varrho$ for any $t > t_m$. Here, the parameter ϱ represents the precision requested, which of course modifies the resulting switching time. In Figure 8.11 we have used the values $\varrho = 1/1000$, 1/300, 1/100, 1/30 and 1/10 and they correspond to the curves from the top to the bottom for both panels. While the switching time of the phase A–D is a monotonically decreasing function of the applied electric field (Figure 8.11(b)), the switching time of the phase B–C reveals a more complex scenario (Figure 8.11(a)). In particular, we observe that in correspondence to the electric field $E^\infty = 9.5 \times 10^6$ V/m there is a transition where the B–C switching time increases considerably. Therefore, the region where $E^\infty > 9.5 \times 10^6$ V/m is not convenient for the memory element. We conclude that the optimal working region (from the switching time point of view) is defined by an electric potential ranging from 0.25 V to 1 V. In fact, in this interval we have $t_m < 0.4$ ns with the better precision defined by $\varrho = 1/1000$.

8.5 Stochastic Error Analysis

We introduce here the statistical mechanics of the magnetization for a single particle by means of the Langevin approach and the Fokker-Planck methodology. We therefore apply these techniques to analyze the thermal effects on the magnetoelectric switching processes of magnetization.

8.5.1 Statistical Mechanics of Magnetization in a Single-Domain Particle

The LLG Equation (8.5) is valid for a system at $T = 0°$ K. It means that it does not consider the effects of the temperature and it must be generalized to implement the nonequilibrium statistical mechanics of the magnetization. We begin by defining a mobile reference frame rigidly connected with the magnetization vector

$$\begin{aligned} \vec{\delta} &= (\cos\varphi\cos\vartheta, \sin\varphi\cos\vartheta, -\sin\vartheta)\,, \\ \vec{\beta} &= (-\sin\varphi, \cos\varphi, 0)\,, \\ \vec{\gamma} &= (\cos\varphi\sin\vartheta, \sin\varphi\sin\vartheta, \cos\vartheta)\,, \end{aligned} \tag{8.14}$$

where ϑ and φ are the standard nutation and precession angles, respectively. Moreover, we observe that $\vec{\delta}$ and $\vec{\beta}$ are orthogonal unit vectors lying on the plane perpendicular to $\vec{\gamma}$. We

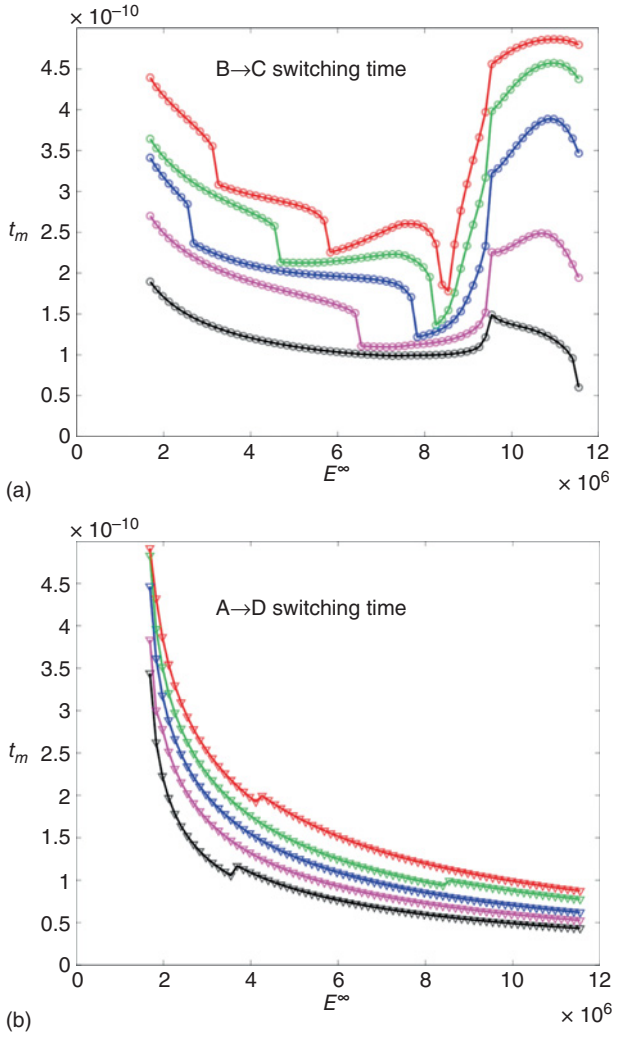

Figure 8.11 Switching times of the commutation phases B–C (a) and A–D (b) as function of the applied electric field E^{∞} in the range 1.7×10^6 V/m-11.5 $\times$ 10^6 V/m (corresponding to the electric potential between 0.22 V and 1.5 V). The different curves (from the top to the bottom) correspond to the values $\varrho = 1/1000, 1/300, 1/100, 1/30$ and $1/10$ of the precision parameter. *Source*: Giordano *et al*., 2012 [50]. Reproduced with permission of the American Physical Society.

can easily prove that Equation (8.5) is equivalent to the following system of differential equations

$$\dot{\varphi} \sin \vartheta = -\frac{\mathcal{G}}{M_s(1+\alpha^2)} \left(\vec{\delta} \cdot \frac{\partial \tilde{w}}{\partial \vec{\gamma}} + \alpha \vec{\beta} \cdot \frac{\partial \tilde{w}}{\partial \vec{\gamma}} \right),$$
$$\dot{\vartheta} = -\frac{\mathcal{G}}{M_s(1+\alpha^2)} \left(-\vec{\beta} \cdot \frac{\partial \tilde{w}}{\partial \vec{\gamma}} + \alpha \vec{\delta} \cdot \frac{\partial \tilde{w}}{\partial \vec{\gamma}} \right). \tag{8.15}$$

Now, since $\partial\vec{\gamma}/\partial\vartheta = \vec{\delta}$ and $\partial\vec{\gamma}/\partial\varphi = \sin\vartheta\vec{\beta}$ we obtain a simpler form where the partial derivatives $\frac{\partial\tilde{w}}{\partial\vartheta}$ and $\frac{\partial\tilde{w}}{\partial\varphi}$ appear explicitly:

$$\begin{aligned}\dot{\varphi}\sin\vartheta &= -\frac{\mathcal{G}}{M_s(1+\alpha^2)}\left(\frac{\partial\tilde{w}}{\partial\vartheta} + \frac{\alpha}{\sin\vartheta}\frac{\partial\tilde{w}}{\partial\varphi}\right),\\ \dot{\vartheta} &= -\frac{\mathcal{G}}{M_s(1+\alpha^2)}\left(-\frac{1}{\sin\vartheta}\frac{\partial\tilde{w}}{\partial\varphi} + \alpha\frac{\partial\tilde{w}}{\partial\vartheta}\right).\end{aligned} \tag{8.16}$$

In order to introduce thermal fluctuations we assume the Brown hypothesis affirming that the effects of the temperature can be mimicked by an addictive random field acting on the magnetization [59–62]. It means that we substitute $\frac{\partial\tilde{w}}{\partial\vec{\gamma}}$ with $\frac{\partial\tilde{w}}{\partial\vec{\gamma}} + \mathcal{D}\vec{n}$ where $\vec{n}$ is a stochastic process with three main properties: its average value is zero at any time, $\langle\vec{n}(t)\rangle = 0$, it is completely uncorrelated (white), $\langle n_i(t)n_j(\tau)\rangle = 2\delta_{ij}\delta(t-\tau)$, and it is Gaussian. So, Equation (8.16) has been generalized by obtaining the Langevin LLG system

$$\begin{aligned}\dot{\varphi}\sin\vartheta &= -\frac{\mathcal{G}}{M_s(1+\alpha^2)}\left[\frac{\partial\tilde{w}}{\partial\vartheta} + \frac{\alpha}{\sin\vartheta}\frac{\partial\tilde{w}}{\partial\varphi} + \mathcal{D}\left(\vec{\delta}+\alpha\vec{\beta}\right)\cdot\vec{n}\right],\\ \dot{\vartheta} &= -\frac{\mathcal{G}}{M_s(1+\alpha^2)}\left[-\frac{1}{\sin\vartheta}\frac{\partial\tilde{w}}{\partial\varphi} + \alpha\frac{\partial\tilde{w}}{\partial\vartheta} + \mathcal{D}\left(\alpha\vec{\delta}-\vec{\beta}\right)\cdot\vec{n}\right].\end{aligned} \tag{8.17}$$

It is well known that the combination of dissipation (friction controlled by the Gilbert damping constant α) and fluctuation (described by the diffusion coefficient $\mathcal{D}$) is able to describe the dynamic transient state leading to the equilibrium thermodynamics for long time [63, 64]. It is a general concept valid both in classical mechanics [65, 66] and in quantum one [67, 68]. The system obtained in Equation (8.17) is a stochastic differential equation (SDE): from the mathematical point of view there are two different approaches for defining the meaning of a SDE, namely, the Itô stochastic calculus and the Stratonovich one [69, 70]. Throughout this chapter we use the Stratonovich approach for two main reasons: first, the usual rules of calculus (for derivatives and integrals) remain unchanged and, second, the Stratonovich approach is the most convenient interpretation within the physical sciences since it can be obtained as the limiting process of a colored noise toward an uncorrelated (white) one [63]. The typical tool for studying SDEs is the Fokker-Planck methodology based on a partial differential equation describing the dynamic of the density probability of the state of the system [63]. In our case the state of the system is given by the couple (φ, ϑ) and, therefore, the density probability can be written as $\rho = \rho(\varphi, \vartheta, t)$. The related Fokker-Planck equation assumes the form

$$\begin{aligned}\frac{\partial\rho}{\partial t} &= \frac{\mathcal{G}}{M_s(1+\alpha^2)\sin\vartheta}\frac{\partial}{\partial\varphi}\left\{\left[\frac{\partial\tilde{w}}{\partial\vartheta} + \frac{\alpha}{\sin\vartheta}\frac{\partial\tilde{w}}{\partial\varphi}\right]\rho\right\}\\ &+ \frac{\mathcal{G}}{M_s(1+\alpha^2)}\frac{\partial}{\partial\vartheta}\left\{\left[-\frac{1}{\sin\vartheta}\frac{\partial\tilde{w}}{\partial\varphi} + \alpha\frac{\partial\tilde{w}}{\partial\vartheta}\right]\rho\right\}\\ &- \frac{\mathcal{G}^2\mathcal{D}^2}{M_s^2(1+\alpha^2)}\frac{\partial}{\partial\vartheta}\left\{\frac{\cos\vartheta}{\sin\vartheta}\rho\right\} + \frac{\mathcal{G}^2\mathcal{D}^2}{M_s^2(1+\alpha^2)}\left\{\frac{1}{\sin^2\theta}\frac{\partial^2\rho}{\partial\varphi^2} + \frac{\partial^2\rho}{\partial\vartheta^2}\right\}.\end{aligned} \tag{8.18}$$

As mentioned above, this equation should have an asymptotic solution coherent with the equilibrium thermodynamics and, therefore, we can verify that

$$\lim_{t\to\infty} \rho\,(\varphi, \vartheta, t) = \frac{\sin\vartheta}{\mathcal{Z}} \exp\left[-\frac{\tilde{w}(\varphi,\vartheta)v}{k_B T}\right], \tag{8.19}$$

where the partition function $\mathcal{Z}$ is given by

$$\mathcal{Z} = \int_0^{\pi}\int_0^{2\pi} \sin\vartheta \exp\left[-\frac{\tilde{w}(\varphi,\vartheta)v}{k_B T}\right] d\varphi d\vartheta. \tag{8.20}$$

Here k_B is the Boltzmann constant and T is the absolute temperature. Note that the term $\sin\vartheta$ in previous expressions is due to the (non-Cartesian) spherical system (it corresponds to the Jacobian of the coordinates transformation). Moreover, v represents the volume of the magnetic particle ($\tilde{w}v$ is the total energy being $\tilde{w}$ the energy density). The value of the diffusion constant $\mathcal{D}$ can be found by substituting Equation (8.19) in Equation (8.18) and by observing that we obtain an identity if and only if

$$\mathcal{D}^2 = \frac{\alpha M_s k_B T}{\mathcal{G}v}, \tag{8.21}$$

an equation representing the specific fluctuation-dissipation property. Once the value of $\mathcal{D}$ is known, we can rewrite the Fokker-Planck equation for $\rho(\varphi, \vartheta, t)$ as follows:

$$\begin{aligned} 2\tau_N \frac{\partial\rho}{\partial t} = {} & \frac{v}{\alpha k_B T}\frac{1}{\sin\vartheta}\frac{\partial}{\partial\varphi}\left\{\left[\frac{\partial\tilde{w}}{\partial\vartheta} + \frac{\alpha}{\sin\vartheta}\frac{\partial\tilde{w}}{\partial\varphi}\right]\rho\right\} + \frac{v}{\alpha k_B T}\frac{\partial}{\partial\vartheta}\left\{\left[-\frac{1}{\sin\vartheta}\frac{\partial\tilde{w}}{\partial\varphi} + \alpha\frac{\partial\tilde{w}}{\partial\vartheta}\right]\rho\right\} \\ & -\frac{\partial}{\partial\vartheta}\left\{\frac{\cos\vartheta}{\sin\vartheta}\rho\right\} + \frac{1}{\sin^2\theta}\frac{\partial^2\rho}{\partial\varphi^2} + \frac{\partial^2\rho}{\partial\vartheta^2}, \end{aligned} \tag{8.22}$$

where we have introduced to so-called Néel time

$$\tau_N = \frac{M_s(1+\alpha^2)v}{2\alpha\mathcal{G}k_B T}, \tag{8.23}$$

representing the characteristic response time of a particle without external fields (see below for details). Since we are working in spherical coordinates it is useful to define another density $\wp(\varphi, \vartheta, t)$ through the relation $\rho(\varphi, \vartheta, t) = \sin\vartheta\wp(\varphi, \vartheta, t)$ (see Equation (8.19) for comparison). So, it is not difficult to obtain the evolution equation of this new function

$$\begin{aligned} 2\tau_N \frac{\partial\wp}{\partial t} = {} & \frac{v}{\alpha k_B T}\frac{1}{\sin\vartheta}\frac{\partial}{\partial\varphi}\left\{\left[\frac{\partial\tilde{w}}{\partial\vartheta} + \frac{\alpha}{\sin\vartheta}\frac{\partial\tilde{w}}{\partial\varphi}\right]\wp\right\} \\ & + \frac{v}{\alpha k_B T}\frac{1}{\sin\vartheta}\frac{\partial}{\partial\vartheta}\left\{\left[-\frac{1}{\sin\vartheta}\frac{\partial\tilde{w}}{\partial\varphi} + \alpha\frac{\partial\tilde{w}}{\partial\vartheta}\right]\sin\vartheta\wp\right\} + \nabla_S^2\wp, \end{aligned} \tag{8.24}$$

where we have defined the surface Laplacian ∇_S^2 (or Laplace-Beltrami operator on a spherical surface) as

$$\nabla_S^2 f = \frac{1}{\sin\vartheta}\frac{\partial}{\partial\vartheta}\left[\sin\vartheta\frac{\partial f}{\partial\vartheta}\right] + \frac{1}{\sin^2\vartheta}\frac{\partial^2 f}{\partial\varphi^2}. \tag{8.25}$$

The obtained Fokker-Planck equations (Equation (8.22) for ρ and Equation (8.24) for $\wp$) are particularly useful for obtaining a simplified version of the Langevin LLG system given in Equation (8.17): in fact, in Equation (8.17) a three-dimensional random vector has been added in order to introduce the fluctuations in a system with two variables (φ and ϑ). There is no need to embed the system in a three-dimensional space and, moreover, there are important reasons for not doing so, such as concerns about the coherence and elegance of the theory and saving of computational resources. We consider the following new version of the Langevin LLG system where only two noise terms are considered [71]

$$\begin{aligned}
\dot{\varphi} &= -\frac{\mathcal{G}}{M_s(1+\alpha^2)\sin\vartheta}\left[\frac{\partial\tilde{w}}{\partial\vartheta} + \frac{\alpha}{\sin\vartheta}\frac{\partial\tilde{w}}{\partial\varphi}\right] + \frac{1}{\sin\vartheta}\sqrt{\frac{1}{2\tau_N}}n_\phi \\
\dot{\vartheta} &= -\frac{\mathcal{G}}{M_s(1+\alpha^2)}\left[-\frac{1}{\sin\vartheta}\frac{\partial\tilde{w}}{\partial\varphi} + \alpha\frac{\partial\tilde{w}}{\partial\vartheta}\right] + \frac{1}{2\tau_N}\frac{\cos\vartheta}{\sin\vartheta} + \sqrt{\frac{1}{2\tau_N}}n_\theta.
\end{aligned} \tag{8.26}$$

If the noises have the standard properties for the average values $\langle n_\phi(t)\rangle = 0$, $\langle n_\theta(t)\rangle = 0$, and for the correlation s $\langle n_\phi(t)n_\theta(\tau)\rangle = 0$, $\langle n_\phi(t)n_\phi(\tau)\rangle = 2\delta(t-\tau)$, $\langle n_\theta(t)n_\theta(\tau)\rangle = 2\delta(t-\tau)$ and they are Gaussian, we can prove that the Fokker-Planck equations established starting from Equation (8.26) are exactly coincident to Equation (8.22) for ρ and to Equation (8.24) for $\wp$. From the theoretical point of view Equation (8.26) is more coherent and elegant since the SDE lives completely on the spherical surface without the need for a three-dimensional embedding: it represents the covariant formulation of the SDE on the spherical manifold [72,73]. Moreover, from the computational point of view Equation (8.26) is convenient since two random numbers must be generated at any time step, instead of the three ones needed for the implementation of Equation (8.17). They can be directly obtained by means of the Box-Muller theorem [74]. Another remarkable advantage of Equation (8.26) is that the noise induced drift term is always zero, yielding exactly the same SDE both for the Itô and the Stratonovich approach. This fact allows us to apply indifferently numerical techniques specifically developed for either the Itô or the Stratonovich interpretation of SDEs.

To conclude, when we approach the problem of studying the thermal effects on the magnetization dynamics of a single particle we can adopt one of the three following methodologies. First, we can take into consideration the Fokker-Planck equation and we can search its solution through the finite difference method or the finite element method. Such a technique has been used to investigate the dependence of the magnetization reversal on temperature, damping and applied fields [75–77]. As a second approach, it is possible to develop the density $\wp(\varphi,\vartheta,t)$ in a series of harmonic functions, $\wp(\varphi,\vartheta,t) = \sum_{n=0}^{\infty}\sum_{m=-n}^{n} c_{nm}(t)Y_{nm}(\varphi,\vartheta)$, and to analyze the dynamics of the coefficients $c_{nm}(t)$. The kinetic equation for these coefficients has been obtained [78–80] and it has been largely used for determining the relaxation time of the Fokker Planck operator [81–84]. Finally, the third approach consists in numerically solving

the Langevin equation and in calculating the relevant average values through the Monte Carlo method [85].

8.5.2 Switching Process within the Magnetoelectric Memory

We can now approach the problem of evaluating the temperature effects on the memory element introduced in Section 8.4.1. As one can find in Table 8.3, at the beginning we have considered an ellipsoidal particle with axes 45, 25 and 20 nm. Nevertheless, we may now consider an arbitrary size of the particle. To explain this point we recall an important property of the Eshelby theory that is valid in any case of coupling: when an ellipsoidal particle is embedded in an infinite matrix and subjected to uniform external actions, the physical fields (electric, magnetic and elastic) induced within the particle itself are always uniform and they depend on the material properties of the two phases and on the ratios a_1/a_2 and a_2/a_3 [44–47, 50, 54, 55]. The internal fields do not depend on the actual size of the particle: only the shape of the ellipsoid may influence the particle response. Therefore, also the results based on the energy function defined in Equation (8.13) are scale invariant and depend only on the ratio between the axes lengths. We conclude that the numerical evaluation of $\tilde{w}$ described in Section 8.4 can be used for any rescaled version of the particle.

The only effect of the real size of the particle is introduced in the Langevin system (see Equation (8.26)) through the Néel time τ_N defined in Equation (8.23). Since $1/\tau_N$ is directly proportional to k_BT/v with a coefficient that is simply material dependent, we can analyze the thermal effects in terms of the ratio k_BT/v, describing the compromise between temperature and particle size. We remark that one of the most important parameter of the system is the energy barrier between the metastable states A and B, which can be observed on Figure 8.9(b), in the absence of an electric field. It is an intrinsic property of the structure depending only on the geometrical and physical anisotropies of the particle and on the externally applied magnetic field creating the quite orthogonal states: with the set of parameters defined in Tables 8.1 and 8.3, for an effective anisotropic field H_a set at 18×10^4 A/m and an external magnetic field H^∞ equal to 50×10^4 A/m, we obtain an energy barrier equal to $\Delta e = 2.5 \times 10^4$ J/m^3. It is evident that the memory can work only if the density of thermal energy k_BT/v is much lower than Δe (for avoiding unwanted switching between the states). For example, for the initially proposed structure ($v \simeq 10^{-22}$ m^3) at room temperature ($T = 300$ °K) we have $k_BT/v = 40$ J/m^3 $\ll \Delta e$ and, therefore, the system should work correctly. In this case the total energy barrier between the states A and B corresponds to $v\Delta e = 1.7 \cdot 10^{-18} J \simeq 400 k_BT$. It is interesting to know how much we can increase the temperature or, on the other hand, decrease the volume of the particle, without modifying the regular operation of the device. In other words, we search for the maximum value of k_BT/v admissible for our structure. In order to do this, we consider the system without an electric field applied to the piezoelectric matrix and we suppose to have an initial magnetization in the state A or B. We observe that the state A is represented by $\vec{\gamma} = \vec{v}_A = (\cos\varphi_A, \sin\varphi_A, 0)$ where $\varphi_A \simeq 0.892$ while for the state B we have $\vec{\gamma} = \vec{v}_B = (\cos\varphi_B, \sin\varphi_B, 0)$ where $\varphi_B \simeq 2.277$. We determine the trajectories of $\vec{\gamma}$ starting from these points in order to analyze the stability of the stored bit. It means that we simulate the transition A $\rightarrow$ A generated by the electric potential change V $= +0.5$ V $\rightarrow V = 0$ V and the transition B $\rightarrow$ B generated by the electric potential change $V = -0.5\,V \rightarrow V = 0$ V. For any value of the ratio k_BT/v (in the range from 10 J/m^3 to 2×10^4 J/m^3) we generate 10 000

trajectories $\vec{\gamma}(t)$ by solving Equation (8.26) (with $E^{\infty} = 0$ and $\vec{\gamma}(0) = \vec{v}_A$ or $\vec{\gamma}(0) = \vec{v}_B$) and we determine the average values through the Monte Carlo method. The numerical solution of Equation (8.26) has been performed through a standard integration scheme with a time step $\delta t = 2.4 \times 10^{-13}$ sec.

The results are reported in Figure 8.12. In Figure 8.12(a) we show the time evolution of the three components of $\langle \vec{\gamma}(t) \rangle$ for 100 different values of the ratio $k_B T/v$. In Figure 8.12(b) one can find the trajectories of the projections $\vec{\gamma} \cdot \vec{v}_A$ and $\vec{\gamma} \cdot \vec{v}_B$, showing more clearly the possible escape from the initial potential well. It is evident that for the larger values of $k_B T/v$ we observe a vector $\langle \vec{\gamma} \rangle$ rapidly aligned to the y-axis, indicating the complete information loss (in this situation we have $\vec{\gamma} \cdot \vec{v}_A \simeq \vec{\gamma} \cdot \vec{v}_B$). A measure of this effect is given by the error probability, shown in Figure 8.12(c). For any value of $k_B T/v$ we follow 10 000 trajectories for a long time and we determine the number of unwanted switching towards the other metastable state. The error probability is given by the ratio between this number and the total number of trajectories (10 000 in our case). We obtained quite the same curve of P_{err} versus $\log_{10}(k_B T/v)$ for both transitions A–A and B–B. It means that the error probability is a symmetric quantity for our system. Moreover, we observe that if $k_B T/v \to +\infty$ then $P_{err} \to 1/2$, a value exactly quantifying the total information loss. We can identify the maximum value admissible for $k_B T/v$ in order to have a negligible error probability ($< 10^{-8}$): we obtain $(k_B T/v)_{max} \simeq 10^3$ J/m^3 [48], which is much larger than our initial proposition (40 J/m^3) and, at the same time, much smaller than the fixed energy barrier between the states ($\Delta e = 2.5 \times 10^4$ J/m^3).

Once determined the restriction on the ratio $k_B T/v$ we may analyze the dynamics of the transitions A–B and B–A. Since we want to analyze the real dynamics at a given temperature we cannot start our simulations at $\vec{\gamma}(0) = \vec{v}_A$ or $\vec{\gamma}(0) = \vec{v}_B$. Instead, we must start with a random initial condition coherent with the statistical distribution within the initial potential well. For any value of $k_B T/v$ in the range from 10 J/m^3 to 4×10^3 J/m^3 we generate 10 000 trajectories of the magnetization and we evaluate their average values. On the left-hand side of Figure 8.13 we show the results for the switching A–B corresponding to the applied traction at $V = -0.5$ V. Similarly, on the right-hand side of Figure 8.13 we show the results for the switching B–A corresponding to the applied compression at V = +0.5 V. In Figure 8.13(a) we present the time behavior of the components of $\langle \vec{\gamma} \rangle$ and in Figure 8.13(b) the projections $\vec{\gamma} \cdot \vec{v}_A$ and $\vec{\gamma} \cdot \vec{v}_B$. The good switching behavior is evident in all whole range of variation of $k_B T/v$. In particular, the regular accomplishment of transitions is well described by the limit $\lim_{t \to \infty} \vec{\gamma} \cdot \vec{v}_B = 1$ for the switching A–B and by $\lim_{t \to \infty} \vec{\gamma} \cdot \vec{v}_A = 1$ for the switching B–A (see Figure 8.13(b)). We note that $\vec{\gamma} \cdot \vec{v}_A$ during the transition A–B and $\vec{\gamma} \cdot \vec{v}_B$ during the transition B–A do not approach zero because of the nonperfect orthogonality of the states. We use this asymptotic behavior to introduce the switching time t_m of the process. It is defined as the first instant of time t_m satisfying the condition $|\vec{\gamma}(t) \cdot \vec{v}_B - \vec{\gamma}(+\infty) \cdot \vec{v}_B| < \varepsilon_\gamma$ for any $t > t_m$ (for the transition A–B). Evidently, for the second transition B–A the inequality reads $|\vec{\gamma}(t) \cdot \vec{v}_A - \vec{\gamma}(+\infty) \cdot \vec{v}_A| < \varepsilon_\gamma$. In Figure 8.13(c) we show the switching time in terms of the ratio $k_B T/v$. The three different set of data correspond to three values of the precision parameter ε_γ. In all cases we observe an increasing trend of t_m versus $k_B T/v$. Nevertheless, the behavior of the curves for the switching A–B and B–A is quite different because of the different physical processes involved. The transition A–B is characterized by a traction inducing an axial anisotropy from the magnetic point of view, while the transition B–A is characterized by a compression inducing a planar anisotropy for the magnetization.

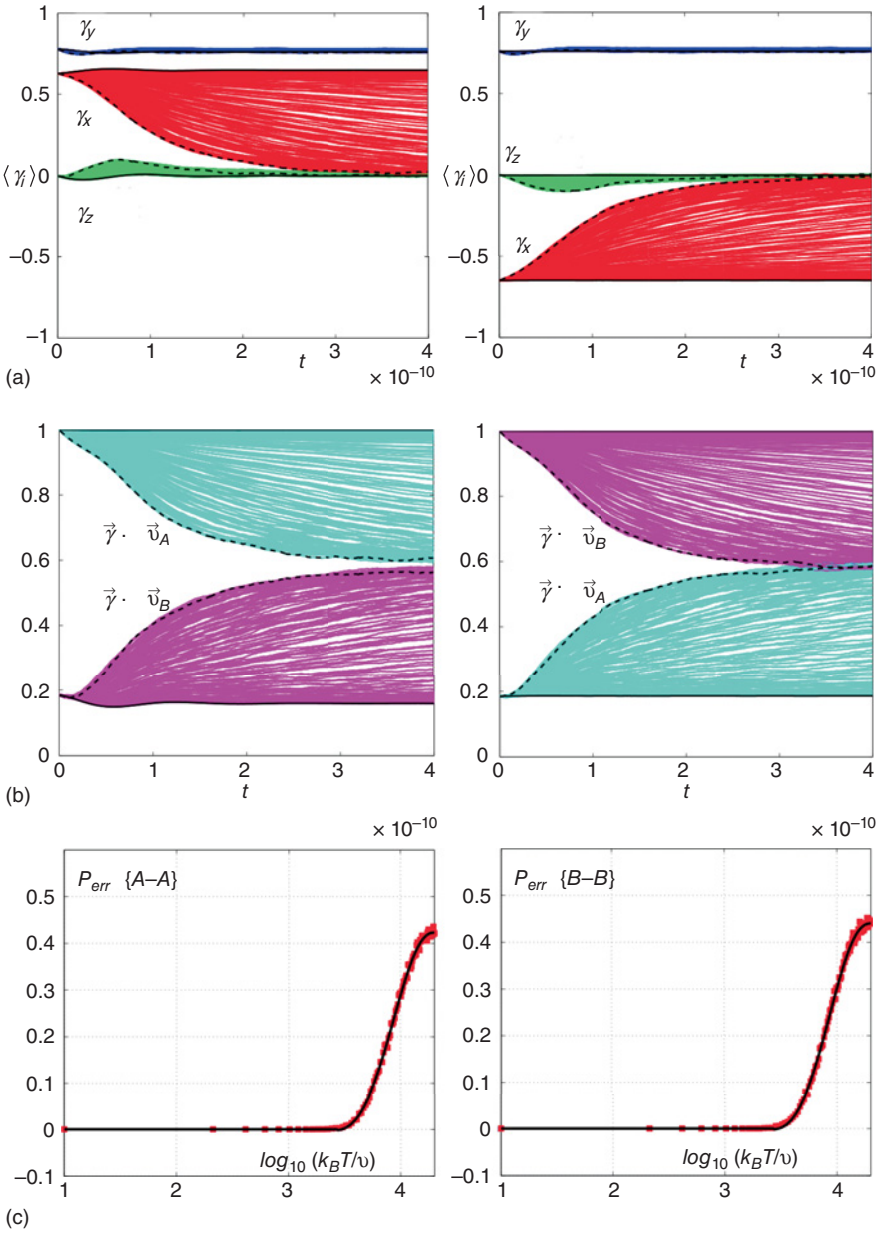

Figure 8.12 Stability analysis of the switching, left: A (V = +0.5 V) − A ($V = 0$ V), right: B ($V = -0.5$ V) − B ($V = 0$ V). First row: trajectories followed by the average magnetization components for different values of k_BT/v (100 equispaced values from 10 J/m^3 to 20 000 J/m^3). The black solid lines correspond to the smallest ratio k_BT/v while the black dashed lines to the highest one. Second row: trajectories followed by the projections $\vec{\gamma} \cdot \vec{v}_A$ and $\vec{\gamma} \cdot \vec{v}_A$. The black lines have the same meaning as in the first row. Third row: error probability in the transition A–A (probability of the switching A–B induced by the temperature) and in the transition B–B (probability of the switching B–A induced by the temperature), in terms of the ratio k_BT/v.

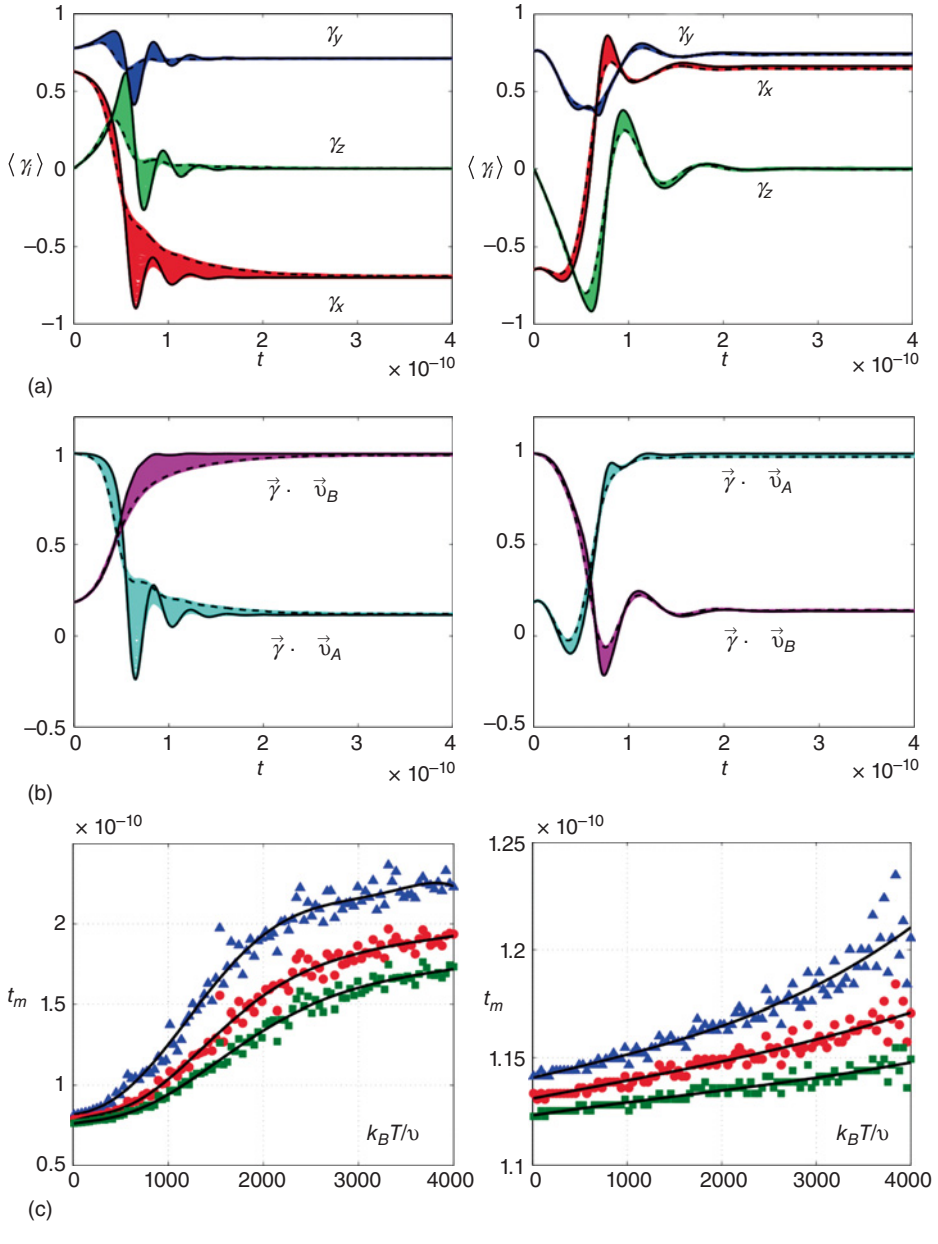

Figure 8.13 Switching process: (*left*) between states A and B (traction, $V = -0.5$ V); (*right*) between states B and A (compression, V = +0.5 V). (a) Trajectories followed by the average magnetization components for different values of k_BT/v (100 equispaced values from 10 J/m^3 to 4000 J/m^3). The black solid lines correspond to the smallest ratio k_BT/v while the black dashed lines to the highest one. (b) Trajectories followed by the projections $\vec{\gamma} \cdot \vec{v}_A$ and $\vec{\gamma} \cdot \vec{v}_B$. The black lines have the same meaning as in the first row. (c) Switching time t_m versus k_BT/v for three different values of the precision parameter (triangles: $\varepsilon_\gamma = 0.01$; circles: $\varepsilon_\gamma = 0.02$; squares: $\varepsilon_\gamma = 0.03$). *Source*: Giordano *et al.*, 2013b [48]. Reproduced by permission of IOP Publishing.

To conclude, we discuss the results concerning the energy consumption during the switching phases. This energy derives from the charge/discharge of the effective capacitor and from the damped precession of the magnetization [20, 86]. The first contribution ΔE_e represents the so-called CV^2 dissipation and it can be simply determined when the geometry of the system is given. For example, if we consider the parameters shown in table we obtain $\Delta E_e = 7.5 \times 10^{-17}$ J. The second contribution ΔE_m can be evaluated by determining the variation of $\tilde{w}(t)$ during the transitions phases. We can obtain the time evolution of $d\tilde{w}(t)/dt$ through the expression $d\tilde{w}(t)/dt = (\partial\tilde{w}/\partial\vartheta)\dot{\vartheta} + (\partial\tilde{w}/\partial\varphi)\dot{\varphi}$ and we can use Equation (8.26) to evaluate the terms $\dot{\vartheta}$ and $\dot{\varphi}$. This procedure can be numerically implemented within the integration scheme of the Langevin system. As before, the average values are determined with the Monte Carlo technique. Since $\tilde{w}$ is always a decreasing function during the switching phases, we show the average value of $-d\tilde{w}(t)/dt$ for the transitions B–A (Figure 8.14(a)) and A–B (Figure 8.14(b)). This is done for 100 equispaced values of k_BT/v (from 10 J/m^3 to 4000 J/m^3). Interestingly enough, we note that the temperature effects are stronger in the transition A–B. However, we can determine the specific energy dissipated during a transition phase by integrating the time derivative of $\tilde{w}$: $\Delta E_m/v = -\int_0^{+\infty} (d\tilde{w}(t)/dt)dt$ (see also Equation (8.9)). The numerical integration leads to the results shown on Figure 8.14(c), where $\Delta E_m/v$ is plotted versus k_BT/v for both transitions B–A and A–B. We observe that there is only a very slight (linear) dependence of $\Delta E_m/v$ on k_BT/v. In fact, we can approximate $\Delta E_m/v \simeq 2 \times 10^5$ J/m^3 for any value of k_BT/v. For our original particle with $v = 10^{-22}$ m^3 we obtain $\Delta E_m = 2 \times 10^{-17}$ J

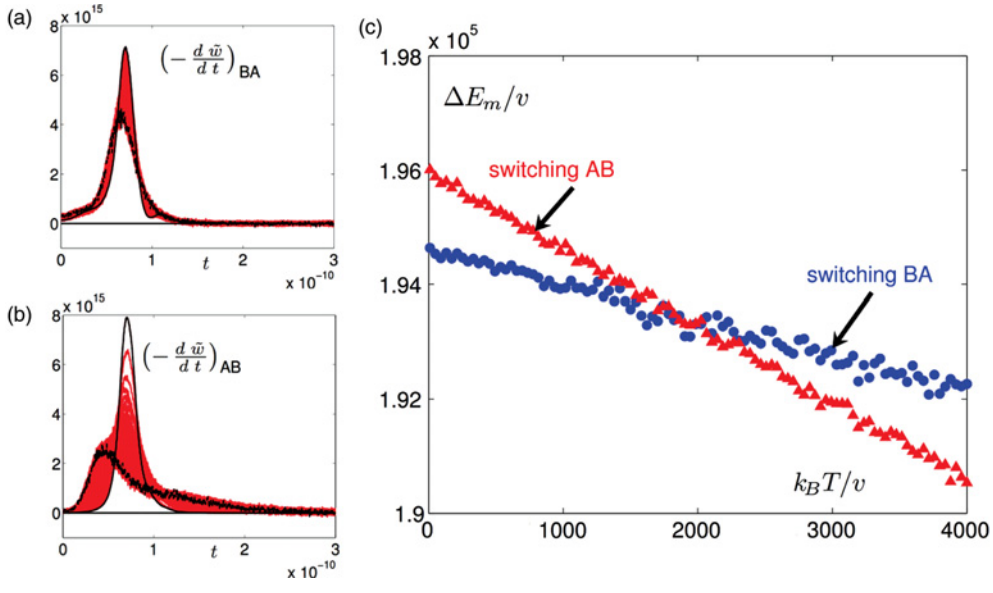

Figure 8.14 Energy dissipation during switching phases. (a) Average value of $-d\tilde{w}/dt$ during the transition B–A for different values of k_BT/v (100 equispaced values from 10 J/m^3 to 4000 J/m^3). The dark continuous line corresponds to the smallest ratio k_BT/v while the black noisy line to the highest one. (b) Average value of $-d\tilde{w}/dt$ during the transition A–B. The dark lines have the same meaning as in the first case. (c) Magnetic dissipated energy $\Delta E_m/v$ in terms of k_BT/v for both transitions A–B (triangles) and B–A (circles). *Source*: Giordano *et al.*, 2013b [48]. Reproduced by permission of IOP Publishing.

and the total switching energy is therefore $\Delta E = \Delta E_e + \Delta E_m \simeq 9.5 \times 10^{-17}$ J. This value is strongly competitive when compared with most nonvolatile memory technologies [2, 50].

8.6 Preliminary Experimental Results

Besides theoretical aspects, prototypes were realized in order to validate the concept of the stress-mediated magnetoelectric memory.

8.6.1 Piezoelectric Actuator with in-Plane Polarization

For integration purposes, and as it is technologically challenging to embed a magnetoelastic particle in an electro-active matrix, it is better to consider magnetoelastic films that can be deposited by conventionnal techniques such as evaporation or sputtering. In the following devices, the film is a highly magnetostrictive $10 \times (TbCo_{2(5nm)}/FeCo_{(5nm)})$ exchange coupled multilayer deposited *via* conventional RF-sputtering. For the switching process to be effective, the applied in-plane stress has to be anisotropic (see Equation (8.4) in Section 8.2.2). One can consider a piezoelectric material with an in-plane polarization and electrodes perpendicular to the $\mathbf{x}'$ axis to generate an in-plane electric field [16]. A deformation is generated along $\mathbf{x}'$ using the d_{33} piezoelectric coefficient, and for a constant volume deformation, an opposite deformation along $\mathbf{y}'$ is created. This principle is used in the prototype described on Figure 8.15(a). It uses a commercial piezoelectric actuator composed of stacked PZT plates with electrodes perpendicular to $\mathbf{x}'$, and coated with a nonconductive layer. The magnetic film is deposited onto the polished side of the substrate through a shadow mask by RF sputtering using a rotary turn table in a Leybold Z550 equipment. The deposition is made under a magnetic field generated by permanent magnets in order to induce a magnetic easy axis (EA) in the desired direction,

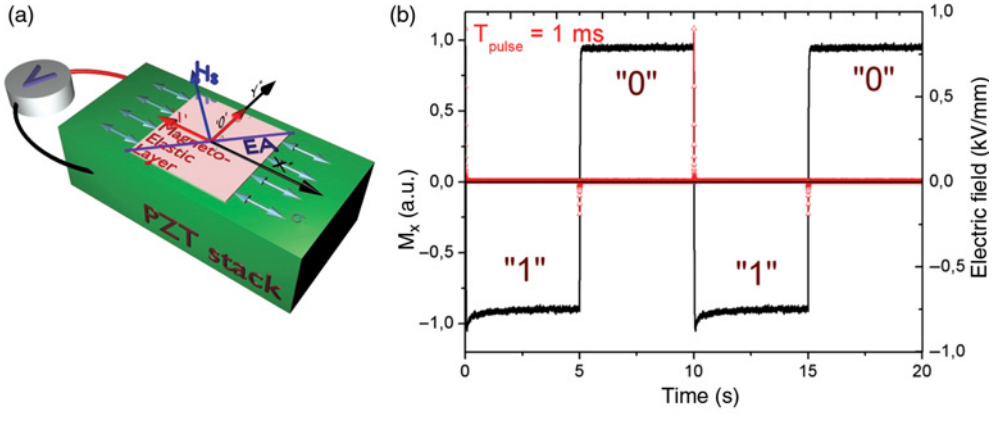

Figure 8.15 (a) Schematic of the demonstrator. The magnetoelastic multilayer is deposited on top of a PZT stack actuator generating stress along the x' direction. (b) MOKE (solid line) evidence of magnetization switching between the two stable states upon application of 1 millisecond positive or negative voltage pulses (triangles) leading respectively to $\sigma > 0$ and $\sigma < 0$. *Source*: Tiercelin *et al.*, 2011a [87]. Reproduced with permission of AIP Publishing LLC.

that is, with an angle of 45° with respect to the $\mathbf{x}'$ axis. The obtained film magnetization was characterized with a Vibrating Sample Magnetometer (VSM) and is characteristic of a uniaxial behavior with an anisotropy field of about $H_a = 160\,000$ A/m. For this kind of layer, the magnetostriction λ_S is measured by laser deflectometry with the clamped beam technique and is about 10^{-4}. The switching was evidenced using a MOKE setup to measure the projection of magnetization along the easy axis, while the polarizing field H was applied on the hard axis, so as to define two stable positions. As shown on the right of Figure 8.15(b), the system behaves as expected. When applying either positive or negative voltage pulses, tensile or compressive stress respectively is generated leading to a switch to "1" or "0." One can also note that the state is kept upon removal of the voltage. Switching was obtained with 1 *ms* pulses, which is the shortest time allowed by the experimental setup.

8.6.2 *Ferroelectric Relaxors with out-of-Plane Polarization*

The solution above is nevertheless not suitable for integrated devices where the active layer has to be inserted into a readout structure and directly in contact with the piezoelectric material. This approach is limited to nonconductive magnetic layers: a conductive film induces a strong distorsion of the electric field lines which have to be perpendicular to the conductor, and therefore leads to improper stress generation. Fortunately, recent advances in the domain of ferroelectric relaxors offer suitable alternatives for out-of-plane polarization. For PMN-PT compositions near the so-called morphotropic phase boundary, 011-cut and poled single crystals exhibit suitable characteristics [88]. A schematic view of the second device is shown on the left-hand side of Figure 8.16(a). The stress is now generated by a commercial PMN-PT substrate that was mechanically polished prior film deposition to ensure a surface smooth enough for MOKE measurements. This time the electric field is applied across the thickness of the active substrate. In the $\mathbf{x}'$, $\mathbf{y}'$, $\mathbf{z}'$ reference, the piezoelectric coefficients are $d_{31} \approx -1900.10^{-12}\ C/N$ and $d_{32} \approx +1000.10^{-12}\ C/N$, which ensures the required anisotropic stress. As in the previous device, MOKE measurements (Figure 8.16(b)) show the evidence of the

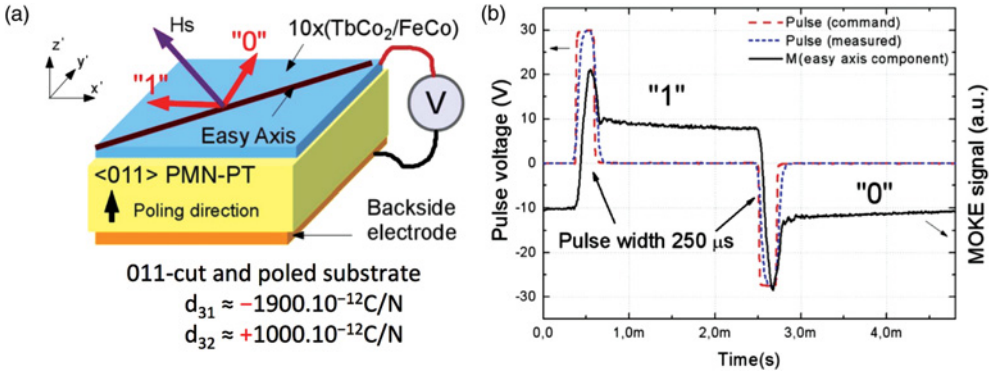

Figure 8.16 (a) Schematic of the demonstrator. The magnetoelastic multilayer is deposited on top of a 011-cut and polarized PMN-PT single crystal. (b) MOKE evidence of magnetization switching between the two stable states upon application of positive or negative voltage pulses leading respectively to $\sigma > 0$ and $\sigma < 0$. *Source*: Dusch *et al.*, 2013 [89]. Reproduced with permission of AIP Publishing LLC.

magnetization switch triggered by voltage pulses. Switching was obtained with 250 µs pulses, which is the shortest time allowed by the experimental setup.

8.6.3 Magnetoelastic Switching in a Magneto-Resistive Structure

The information stored in the memory cell has to be electrically readable. As it is stored magnetically, a magnetoresistive structure is the most suitable option. For a Giant Magneto-Resistance (GMR) or Magnetic Tunnel Junction (MTJ)-based reading strategy, the "memory" layer has to be associated to a "reference" layer with a pinned magnetization so that the switch from one state to the other induces a sufficient magnetoresistive contrast. Such an approach and the influence of stress on spintronic structures have already been studied extensively to assess the influence of technological hazards or the potentialities for stress/strain sensors. In particular, Lohndorf *et al*. detailed the use of a magnetostrictive layer as part of GMR or Magnetic Tunnel Junctions (MTJ) spintronic structures for applications in sensor arrays [90, 91]. However, in our case, the external magnetic field used to define the equilibrium positions of magnetization influences both the free layer and the fixed layer through the Zeeman interaction. Techniques must therefore be found to ensure the magnetoresistance contrast between the two stable positions. We therefore developed a technique based on two nanostructured magnetostrictive layers with exhibiting two different tailored anisotropies, for both the memory layer and the fixed layer of a current-in-plane GMR structure (CIP-GMR). From the theoretical work led in previous sections, we show that given the strength of the anisotropy field $H_{a,eq}$ of the memory element, the polarizing field H must have a minimum strength of $H = H_a/\sqrt{2}$ for the switch between stable positions to be possible. Thus the principle of the proposed device: a layer with a "low" anisotropy field H_{a1} will serve as the memory layer, whereas another with a "high" anisotropy H_{a2} will act as a reference. Setting the polarizing field H at $H_{a1}/\sqrt{2}$ and therefore much lower than H_{a2} will ensure that the reference layer will not switch during the writing operations in the memory layer. In order to tailor the magnetic properties [92–94], elementary layers of highly magnetostrictive $TbCo_2$ alloy are combined with layers of softer $FeCo$: changing the thickness ratio of these exchange coupled layers allows an adjustment of the resulting anisotropy field. The considered stack is thus $FeCo_{(2nm)}/TbCo_{2(6nm)}/FeCo_{(2nm)}/Cu_{(3nm)}/FeCo_{(2nm)}/TbCo_{2(4nm)}/FeCo_{(2nm)}$. With such an arrangement of layers, the two magnetic trilayers that are separated by copper have different equivalent anisotropy fields H_{a1} and H_{a2} that can be estimated using the VSM measurements shown on Figure 8.17(c). The stack was submitted to stress using the device shown in Figure 8.17(a) and (b). As expected, upon tensile stress, the magnetization M_{mem} of the memory layer will switch to the "1" state along the $\mathbf{x}'$ axis, whereas compressive stress will force a switch toward the "0" state along the $\mathbf{y}'$ axis (Figure 8.17(d)). The reference layer M_{ref} does not switch, and thus a contrast in the magnetoresistance is observed [95]. It is to be noted that the resistance contrast between "1" and "0" is inverted when reversing the direction of the reference layer prior to the experiment, thus indicating that we don't observe a simple piezoresistive effect.

8.7 Conclusions

Magneto-electro-elastic materials represent a large class of structures with promising applications in modern nanoscience and nanotechnology. The cross coupling between polarization

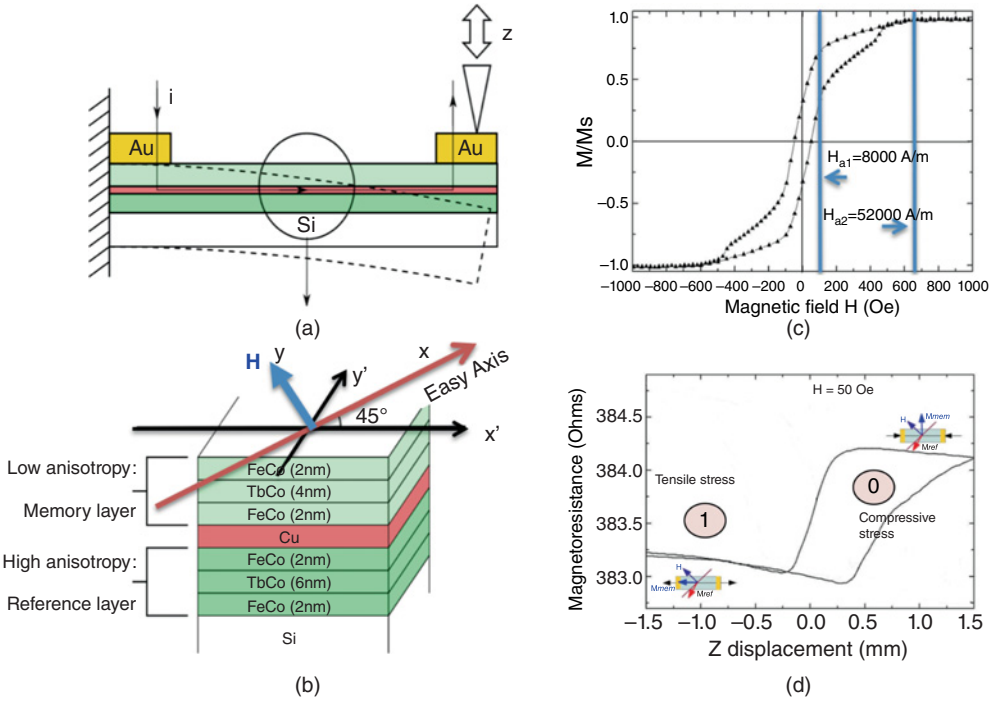

Figure 8.17 (a) Schematic of the magnetoresistive demonstrator. (b) A magnetoresistive stack composed of two magnetoelastic trilayers with different anisotropies and separated by a copper spacer is sputtered onto a silicon cantilever. The tip of the cantilever is displaced along the **z** axis to induce compressive ($\sigma < 0$) or tensile ($\sigma > 0$) stress in the magnetic layer. (c) Magnetization loop along the hard axis showing two anisotropy fields H_{a1} and H_{a2}. (d) Resistance of the device measured between the gold contacts. The resistance reflects the switch of the magnetization in the memory layer M_{mem}. The reference layer M_{ref} does not switch.

and magnetization can be measured in single multiferroic phases or in composites. However, the magneto electric coupling is weak in single phase systems and therefore we turned to composite structures that offer the possibility of strong interactions at room temperature. While the magnetoelectric coupling in laminated systems has been largely studied both experimentally [14] and theoretically in the linear [96, 97] and nonlinear [98] regimes, the exploitation of the magnetization dynamics in single domain particles is a very recent application with important applications in memories, spintronics and new paradigms of information processing.

In these systems, the magnetization dynamics are described by the classical Landau-Lifshitz-Gilbert equation and, through the magnetoelasticity, are strongly influenced by external mechanical stresses applied to the structure. Typically, such mechanical actions are generated by piezoelectric or ferroelectric relaxor based actuators coupled to the magnetic particle. This kind of magneto-electric effect can be carefully controlled in order to obtain the desired behavior and performances. When properly designed, magnetization of the device can be controlled with very high efficiency. As with CMOS-based devices, the main source of energy consumption is still due to the Joule heating during the charge and discharge of capacitances

that lead to a loss of CV^2 for every cycle. But the driving voltages reduction does not suffer from the same limitations. With an equivalent capacitance in the femtofarrad range, a 100 mV driving voltage offers a 50 fold reduction of consumption compared to a 700 mV CMOS device. Research efforts are currently made on the downscaling of the concept. So far, very few stress- or strain-mediated devices have ever been realized at a submicrometer range. It is a necessary step to understand whether this technology is viable or not, and will also provide a valuable tool to understand the multiphysic couplings occuring at lower scales. In fact, when we work with structures displaying their geometry at the nanoscale, several kind of scale effects can be observed and strongly influence the normal behavior of the system. Typically, the scale effects are mediated by the imperfect interfaces which play an important role because of the high surface/volume ratio. Therefore, for analysing nanostructures, we cannot assume perfect interfaces as we did throughout the chapter, but we must consider all possible imperfections leading to considerable nanoscale effects. The concepts of such stress-mediated magnetoelectric devices are not limited to the case of a bi-stable memory. In the past few years, and still in the frame of the "beyond CMOS" electronics, there has been a renewed interest in bio-inspired architectures for information processing. Current models and simulations involve artificial neuron networks that are interconnected with synapses that exhibit plasticity and thus present learning capabilities. Such a network requires an artificial synapse that is not readily available so far. It has been shown, however, that a component exhibiting so called "memristive" properties, that is, that possess an impedance that remembers its history, could be a suitable candidate for the artificial synapse. Thanks to the inherent hysteretic behavior, magneto-electric devices are interesting candidates to realize a memristor. In order to develop magneto-elasto-resistive structures, it is possible to consider the embedding of magnetoelastic materials in magneto-resistive structures such as Giant Magneto Resistance – GMR pillars or Magnetic Tunnnel Junctions – MTJs. A possible structure is composed of a ferroelectric relaxor substrate and a magnetoresistive multilayer. This latter can be considered as formed by two regions separated by an oxide controlling the tunnneling effect. The first region has a fixed magnetization, while the second one, near the ferroelectric material, has a free magnetization, which can easily be oriented by external actions. It is well known that a current flowing in this device feels an electric resistance depending on the angle between the magnetization vectors in the two regions introduced above. On the other hand, the elastic strain imposed by the piezoelectric substrate strongly influences the magnetization of the soft region, finally modifying the overall resistance. We conclude therefore by observing that magneto-electric coupling can also be used to produce resistive structures with possible hysteretic/memory behavior. Magnetoelectric devices are consequently good candidates to realize memristors mimicking the neuronal update rule found in many biological synapses [99].

Acknowledgments

The authors would like to thank: The Direction Générale de l'Armement (DGA-France) for the PhD funding of Dr Y. Dusch; the Agence Nationale de la Recherche (ANR-France) through the PNano NAMAMIS project; the Russian Federation Ministry of Education and Sciences (project N. 2011-1.9-519-021-141 & Contract No. 11.519.11.3023); the Nanomaterials Program of the Russian Academy of Science (RAS); the Russian Foundation for Basic Research (RFBR-Russia) through the 13-02-93105-NCNIL and 13-02-93106-NCNIL

projects; the French Embassy in Moscow (MAE); the Région Nord-Pas-de-Calais through the CPER-CIA program; the "Fondation Centrale Initiatives" under project "Continuum approach for studying the static and dynamic behavior of piezo-magneto-elastic composite materials"; the PRES Lille Nord de France; The Université de Lille I through the BQR-CMAN project and the RENATECH network for promotion of nanotechnologies.

References

[1] ITRS (2013) Emerging research devices. Technical report, *The International Technology Roadmap for Semiconductors*.

[2] Kryder, M. and Kim, C. (2009) After hard drives-what comes next? *IEEE Transactions on Magnetics*, **45**, 3406–3413.

[3] Spaldin, N.A. and Fiebig, M. (2005) Materials science: the renaissance of magnetoelectric multiferroics. *Science*, **309** (5733), 391–392.

[4] Fiebig, M. (2005) Revival of the magnetoelectric effect. *Journal of Physics D: Applied Physics*, **38** (8), R123–R152.

[5] Chiabrera, A., Zitti, E.D., Costa, F., and Bisio, G.M. (1989) Physical limits of integration and information processing in molecular systems. *Journal of Physics D: Applied Physics*, **22** (11), 1571–1579.

[6] Salahuddin, S. and Datta, S. (2007) Interacting systems for self-correcting low power switching. *Applied Physics Letters*, **90** (9), 093503-1–093503-4.

[7] Gajek, M., Bibes, M., Fusil, S., *et al.* (2007) Tunnel junctions with multiferroic barriers. *Nature Materials*, **6** (4), 296–302.

[8] Borisov, P., Hochstrat, A., Chen, X., *et al.* (2005) Magnetoelectric switching of exchange bias. *Physical Review Letters*, **94** (11), 117203-1–117203-4.

[9] Chen, X., Hochstrat, A., Borisov, P., and Kleemann, W. (2006) Magnetoelectric exchange bias systems in spintronics. *Applied Physics Letters*, **89** (20), 202508-1–202508-3.

[10] He, X., Wang, Y., Wu, N., *et al.* (2010) Robust isothermal electric control of exchange bias at room temperature. *Nature Materials*, **9** (7), 579–585.

[11] Duan, C.G., Velev, J.P., Sabirianov, R.F., *et al.* (2008) Surface magnetoelectric effect in ferromagnetic metal films. *Physical Review Letters*, **101** (13), 137201-1–137201-11.

[12] Maruyama, T., Shiota, Y. and Nozaki, T., *et al.* (2009) Large voltage-induced magnetic anisotropy change in a few atomic layers of iron. *Nature Nanotechnology*, **4** (3), 158–161.

[13] Van den Boomgaard, J. and vanRun, A. (1976) Poling of a ferroelectric medium by means of a built-in space charge field, with special reference to sintered magnetoelectric composites. *Solid State Communications*, **19** (5), 405–407.

[14] Nan, C.W., Bichurin, M.I., Dong, S., *et al.* (2008) Multiferroic magnetoelectric composites: historical perspective, status, and future directions. *Journal of Applied Physics*, **103** (3), 031101–031135.

[15] Weiler, M., Brandlmaier, A., Geprags, S., *et al*. (2009) Voltage controlled inversion of magnetic anisotropy in a ferromagnetic thin film at room temperature. *New Journal of Physics*, **11** (1), 013021-1–013021-16.

[16] Hu, J.M. and Nan, C.W. (2009) Electric-field-induced magnetic easy-axis reorientation in ferromagnetic/ferroelectric layered heterostructures. *Physical Review B*, **80** (22), 224416-1–224416-11.

[17] Hockel, J.L., Bur, A., Wu, T., *et al.* (2012) Electric field induced magnetization rotation in patterned ni ring/pb(mg1/3nb2/3)o3](1-0.32)-[pbtio3]0.32 heterostructures. *Applied Physics Letters*, **100** (2), 022401-1–022401-3.

[18] Hockel, J.L., Pollard, S.D., Wetzlar, K.P., *et al.* (2013) Electrically controlled reversible and hysteretic magnetic domain evolution in nickel film/pb(mg1/3nb2/3)o3]0.68-[pbtio3]0.32 (011) heterostructure. *Applied Physics Letters*, **102** (24), 242901-1–242901-5.

[19] Wang, Z., Zhang, Y., Viswan, R., *et al.* (2014) Electrical and thermal control of magnetic coercive field in ferromagnetic/ferroelectric heterostructures. *Physical Review B*, **89** (3), 035118-1–035118-5.

[20] Roy, K., Bandyopadhyay, S., and Atulasimha, J. (2011) Switching dynamics of a magnetostrictive single-domain nanomagnet subjected to stress. *Physical Review B*, **83** (22), 224412-1–224412-15.

[21] Novosad, V., Otani, Y., Ohsawa, A., *et al.* (2000) Novel magnetostrictive memory device. *Journal of Applied Physics*, **87** (9), 6400–6402.
[22] Overby, M., Chernyshov, A., Rokhinson, L.P., *et al.* (2008) Gamnas-based hybrid multiferroic memory device. *Applied Physics Letters*, **92** (19), 192501–192503.
[23] Hu, J.M., Li, Z., Wang, J., *et al.* (2010) A simple bilayered magnetoelectric random access memory cell based on electric-field controllable domain structure. *Journal of Applied Physics*, **108**(4), 043909-1–043909-6.
[24] Clark, A.E. (1974) Magnetic and magnetoelastic properties of highly magnetostrictive rare earth-iron laves phase compounds. *AIP Conference Proceedings*, **18** (1), 1015–1029.
[25] Du Trémolet de Lacheisserie, E. 1993 *Magnetostriction: Theory and Applications of Magnetoelasticity*. CRC, Boca Raton Florida, pp. 53–55.
[26] West, F.G. (1964) Uniaxial anisotropy due to magnetoelastic energy in constrained polycrystalline films. *Journal of Applied Physics*, **35** (6), 1827–1840.
[27] Dewar, G. (1997) Effect of the large magnetostriction of terfenol-d on microwave transmission. *Journal of Applied Physics*, **81** (8), 5713–5715.
[28] Huang, Y.Y. and Jin, Y.M. (2008) Phase field modeling of magnetization processes in growth twinned terfenol-d crystals. *Applied Physics Letters*, **93** (14), 142504-1–142504-3.
[29] Klimov, A., Ignatov, Y., Tiercelin, N., *et al.* (2010) Ferromagnetic resonance and magnetoelastic demodulation in thin active films with an uniaxial anisotropy. *Journal of Applied Physics*, **107** (9), 093916-1–093916-6.
[30] Kobayashi, T. (2005) Damping parameter and wall velocity of re-tm films. *IEEE Transactions on Magnetics*, **41** (10), 2848–2850.
[31] Néel, L. (1949) Théorie du traînage magnétique des ferromagnétiques en grains fins avec applications aux terres cuites. *Annals of Geophysics*, **5**, 99–136.
[32] Brown, W.F. (1963a) Thermal fluctuations of a single-domain particle. *Physical Review*, **130**, 1677–1686.
[33] Chiba, D., Nakatani, Y., Matsukura, F., and Ohno, H. (2010) Simulation of magnetization switching by electric-field manipulation of magnetic anisotropy. *Applied Physics Letters*, **96** (19), 192506-1–192506-3.
[34] Scholz, W., Fidler, J., Schrefl, T., *et al.* (2003) Scalable parallel micromagnetic solvers for magnetic nanostructures. *Computational Materials Science*, **28** (2), 366–383.
[35] Laudau, L. and Lifshitz, E. (1935) On the theory of the dispersion of magnetic permeability in ferromagnetic bodies. *Physikalische Zeitschrift der Sowjetunion*, **8**, 153–169.
[36] Gilbert, T. (2004) Classics in magnetics a phenomenological theory of damping in ferromagnetic materials. *IEEE Transactions on Magnetics*, **40**, 3443–3449.
[37] Lakshmanan, M. (2011) The fascinating world of the landau-lifshitz-gilbert equation: an overview. *Philosophical Transactions of the Royal Society A: Mathematical, Physical and Engineering Sciences*, **369** (1939), 1280–1300.
[38] Beleggia, M., Graef, M.D., Millev, Y.T., *et al.* (2005) Demagnetization factors for elliptic cylinders. *Journal of Physics D: Applied Physics*, **38** (18), 3333–3342.
[39] Quandt, E. (1997) Giant magnetostrictive thin film materials and applications. *Journal of Alloys and Compounds*, **258** (1–2), 126–132.
[40] Tiercelin, N., Pernod, P., Preobrazhensky, V., *et al.* (2000a) Non-linear actuation of cantilevers using giant magnetostrictive thin films. *Ultrasonics*, **38** (1–8), 64–66.
[41] Hindmarsh, A.C. (1983) ODEPACK, A Systematized Collection of ODE Solvers, R. S. Stepleman *et al*. (eds.), North-Holland, Amsterdam, (vol. 1 of), pp. 55–64. *IMACS Transactions on Scientific Computation*, **1**, 55–64.
[42] Tiercelin, N., Dusch, Y., Preobrazhensky, V., and Pernod, P. (2011b) Magnetoelectric memory using orthogonal magnetization states and magnetoelastic switching. *Journal of Applied Physics*, **109** (7), 07D726-1–07D726-3.
[43] Miltat, J., Albuquerque, G. and Thiaville, A. 2002 An introduction to micromagnetics in the dynamic regime. in *Spin Dynamics in Confined Magnetic Structures I*, Springer, pp. 1–33.
[44] Eshelby, J.D. (1957) The determination of the elastic field of an ellipsoidal inclusion, and related problems. *Proceedings of the Royal Society of London. Series A. Mathematical and Physical Sciences*, **241** (1226), 376–396.
[45] Li, J.Y. and Dunn, M.L. (1998) Anisotropic coupled-field inclusion and inhomogeneity problems. *Philosophical Magazine A*, **77** (5), 1341–1350.
[46] Huang, J.H., Chiu, Y.H., and Liu, H.K. (1998) Magneto-electro-elastic eshelby tensors for a piezoelectric-piezomagnetic composite reinforced by ellipsoidal inclusions. *Journal of Applied Physics*, **83** (10), 5364–5370.
[47] Mikata, Y. (2001) Explicit determination of piezoelectric eshelby tensors for a spheroidal inclusion. *International Journal of Solids and Structures*, **38** (40–41), 7045–7063.

[48] Giordano, S., Dusch, Y., Tiercelin, N., *et al.* (2013b) Thermal effects in magnetoelectric memories with stress-mediated switching. *Journal of Physics D: Applied Physics*, **46** (32), 325002-1–325002-12.
[49] Daniel, L., Hubert, O., Buiron, N., and Billardon, R. (2008) Reversible magneto-elastic behavior: a multiscale approach. *Journal of the Mechanics and Physics of Solids*, **56** (3), 1018–1042.
[50] Giordano, S., Dusch, Y., Tiercelin, N., *et al.* (2012) Combined nanomechanical and nanomagnetic analysis of magnetoelectric memories. *Physical Review B*, **85** (15), 155321-1–155321-14.
[51] Giordano, S. and Palla, P.L. (2008) Dielectric behavior of anisotropic inhomogeneities: interior and exterior point eshelby tensors. *Journal of Physics A: Mathematical and Theoretical*, **41** (41), 415205-1–155321-24.
[52] Giordano, S. (2003) Effective medium theory for dispersions of dielectric ellipsoids. *Journal of Electrostatics*, **58** (1–2), 59–76.
[53] Heinonen, E., Juuti, J., and Leppävuori, S. (2005) Characterization and modelling of 3d piezoelectric ceramic structures with atila software. *Journal of the European Ceramic Society*, **25** (12), 2467–2470.
[54] Huang, J.H. and Kuo, W.S. (1997) The analysis of piezoelectric/piezomagnetic composite materials containing ellipsoidal inclusions. *Journal of Applied Physics*, **81** (3), 1378–1386.
[55] Colombo, L. and Giordano, S. (2011) Nonlinear elasticity in nanostructured materials. *Reports on Progress in Physics*, **74** (11), 116501-1–116501-35.
[56] Palla, P.L., Giordano, S., and Colombo, L. (2008) Interfacial elastic properties between *a*-Si and *c*-Si. *Physical Review B*, **78** (1), 012105-1–012105-4.
[57] Palla, P.L., Giordano, S., and Colombo, L. (2009) Interface elasticity in nanostructured silicon. *Physical Review B*, **80** (5), 054105-1–054105-7.
[58] Palla, P.L., Giordano, S., and Colombo, L. (2010) Lattice model describing scale effects in nonlinear elasticity of nanoinhomogeneities. *Physical Review B*, **81** (21), 214113-1–214113-10.
[59] Brown, W.J. (1979) Thermal fluctuation of fine ferromagnetic particles. *IEEE Transactions on Magnetics*, **15** (5), 1196–1208.
[60] Brown, W.F. (1959) Relaxational behavior of fine magnetic particles. *Journal of Applied Physics*, **30** (4), S130–S132.
[61] Brown, W.F. (1963b) Thermal fluctuations of a single domain particle. *Journal of Applied Physics*, **34** (4), 1319–1320.
[62] Brown, W.F. (1963c) Thermal fluctuations of a single-domain particle. *Physical Review*, **130** (5), 1677–1686.
[63] Risken, H. (1989) *The Fokker-Planck-Equation. Methods of Solution and Applications*, 2nd edn, Springer-Verlag, Berlin.
[64] Coffey, W., Kalmykov, Y., and Waldron, J. (2004) *The Langevin Equation: With Applications to Stochastic Problems in Physics, Chemistry, and Electrical Engineering*. World Scientific.
[65] Uhlenbeck, G.E. and Ornstein, L.S. (1930) On the theory of the brownian motion. *Physical Review*, **36** (5), 823–841.
[66] Wang, M.C. and Uhlenbeck, G.E. (1945) On the theory of the brownian motion ii. *Reviews of Modern Physics*, **17** (2–3), 323–342.
[67] Caldirola, P. and Lugiato, L. (1982) Connection between the schrödinger equation for dissipative systems and the master equation. *Physica A: Statistical Mechanics and its Applications*, **116** (12), 248–264.
[68] Bianco, B., Moggia, E., Giordano, S., *et al.* (2001) Friction and noise in quantum mechanics: a model for the interactions between a system and a thermal bath. *Il Nuovo Cimento*, **116**, 155–167.
[69] Schuss, Z. (1980) *Theory and Applications of Stochastic Differential Equations*, John Wiley & Sons, Inc., New York.
[70] Schuss, Z. (2009) *Theory and Applications of Stochastic Processes: An Analytical Approach*, Springer, New York.
[71] Giordano, S., Dusch, Y., Tiercelin, N., *et al.* (2013a) Stochastic magnetization dynamics in single domain particles. *European Physical Journal B: Condensed Matter Physics*, **86** (6), 249-1–249-11.
[72] Bertotti, G., Mayergoyz, I., and Serpico, C. (2009) *Nonlinear Magnetization Dynamics in Nanosystems*. Elsevier.
[73] Fredkin, D. (2001) Brownian motion on manifolds, with application to thermal magnetization reversal. *Physica B: Condensed Matter*, **306** (1–4), 26–32.
[74] Box, G.E.P. and Muller, M.E. (1958) A note on the generation of random normal. *Annals of Mathematical Statistics*, **29** (2), 610–611.
[75] Fukushima, H., Uesaka, Y., Nakatani, Y., and Hayashi, N. (2002a) Dependence of switching time on temperature, applied field, and material parameters. *IEEE Transactions on Magnetics*, **38** (5), 2394–2396.

[76] Fukushima, H., Uesaka, Y., Nakatani, Y., and Hayashi, N. (2002b) Numerical solutions of the fokker-planck equation by the finite difference method for the thermally assisted reversal of the magnetization in a single-domain particle. *Journal of Magnetism and Magnetic Materials*, **242–245, Part 2** (0), 1002–1004.

[77] Fukushima, H., Uesaka, Y., Nakatani, Y., and Hayashi, N. (2004) Effects of damping constant and gyromagnetic term on switching time of single-domain particle. *Journal of Magnetism and Magnetic Materials*, **272–276, Part 1**, 745–746.

[78] Kalmykov, Y.P. (1996) Rotational brownian motion in an external potential: the langevin equation approach. *Journal of Molecular Liquids*, **69**, 117–131.

[79] Coffey, W. and Geoghegan, L. (1996) Differential recurrence relations for the fokker-planck equation for magnetic after-effect and dielectric relaxation in non axially symmetric potentials. *Journal of Molecular Liquids*, **69** (0), 53–81.

[80] Kalmykov, Y.P. and Titov, S.V. (1999) Matrix elements of the system of moment equations governing the kinetics of superparamagnetic particles. *Physical Review Letters*, **82** (14), 2967–2970.

[81] Coffey, W., Garanin, D., Kachkachi, H., and McCarthy, D. (2000) Interpolation formulae between axially symmetric and non-axially symmetric kramers escape rates for single-domain ferromagnetic particles in the intermediate to high-damping limit. *Journal of Magnetism and Magnetic Materials*, **221**, 110–123.

[82] Déjardin, P.M., Crothers, D.S.F., Coffey, W.T., and McCarthy, D.J. (2001) Interpolation formula between very low and intermediate-to-high damping kramers escape rates for single-domain ferromagnetic particles. *Physical Review E*, **63** (2), 021102-1–021102-12.

[83] Kalmykov, Y.P., Coffey, W.T., Ouari, B., and Titov, S.V. (2005) Damping dependence of the magnetization relaxation time of single-domain ferromagnetic particles. *Journal of Magnetism and Magnetic Materials*, **292** (0), 372–384.

[84] Ouari, B. and Kalmykov, Y.P. (2006) Dynamics of the magnetization of single domain particles having tri-axial anisotropy subjected to a uniform dc magnetic field. *Journal of Applied Physics*, **100** (12), 123912-1–123912-10.

[85] Garcia, V. a-Palacios, J.L. and Lazaro, F.J. (1998) Langevin-dynamics study of the dynamical properties of small magnetic particles. *Physical Review B*, **58** (22), 14937–14958.

[86] Roy, K., Bandyopadhyay, S., and Atulasimha, J. (2012) Energy dissipation and switching delay in stress-induced switching of multiferroic nanomagnets in the presence of thermal fluctuations. *Journal of Applied Physics*, **112** (2), 023914-1–023914-8.

[87] Tiercelin, N., Dusch, Y., Klimov, A., *et al.* (2011a) Room temperature magnetoelectric memory cell using stress-mediated magnetoelastic switching in nanostructured multilayers. *Applied Physics Letters*, **99** (19), 192507-1–192507-3.

[88] Wang, F., Luo, L., Zhou, D., *et al.* (2007) Complete set of elastic, dielectric, and piezoelectric constants of orthorhombic $(0.71Pb(Mg_{1/3}Nb_{2/3})O_3{-}0.29PbTiO_3)$ single crystal. *Applied Physics Letters*, **90** (21), 212903-1–212903-3.

[89] Dusch, Y., Tiercelin, N., Klimov, A., *et al.* (2013) Stress-mediated magnetoelectric memory effect with uni-axial tbco2/feco multilayer on 011-cut pmn-pt electrostrictive material. *Journal of Applied Physics*, **113**, 17C719-1–17C719-3.

[90] Lohndorf, M., Duenas, T., Ludwig, A., *et al.* (2002a) Strain sensors based on magnetostrictive gmr/tmr structures. *IEEE Transactions on Magnetics*, **38** (5), 2826–2828.

[91] Lohndorf, M., Duenas, T., Tewes, M., *et al.* (2002b) Highly sensitive strain sensors based on magnetic tunneling junctions. *Applied Physics Letters*, **81** (2), 313–315.

[92] Tiercelin, N., BenYoussef, J., Preobrazhensky, V., *et al.* (2002) Giant magnetostrictive superlattices: from spin reorientation transition to mems. static and dynamical properties. *Journal of Magnetism and Magnetic Materials*, **249** (3), 519–523.

[93] BenYoussef, J., Tiercelin, N., Petit, F., *et al.* (2002) Statics and dynamics in giant magnetostrictive $Tb_xFe_{1-x}{-}Fe_{0.6}Co_{0.4}$ multilayers for mems. *IEEE Transactions on Magnetics*, **38** (5), 2817–2819. DOI: 10.1109/TMAG.2002.803568

[94] Tiercelin, N., Preobrazhensky, V., Pernod, P., *et al.* (2000b) Sub-harmonic excitation of a planar magneto-mechanical system by means of giant magnetostrictive thin films. *Journal of Magnetism and Magnetic Materials*, **210** (1–3), 302–308.

[95] Dusch, Y., Rudenko, V., Tiercelin, N., *et al.* (2012) Hysteretic magnetoresistance in stress controlled magnetic memory device. *Nanomatériaux et nanostructures*, **2**, 44–50.

[96] Sixto-Camacho, L.M., Bravo-Castillero, J., Brenner, R., *et al.* (2013) Asymptotic homogenization of periodic thermo-magneto-electro-elastic heterogeneous media. *Computers & Mathematics with Applications*, **66**(10), 2056–2074.

[97] Giordano, S., Goueygou, M., Tiercelin, N., *et al.* (2014) Magneto-electro-elastic effective properties of multi-layered artificial multiferroics with arbitrary lamination direction. *International Journal of Engineering Science*, **78** (0), 134–153.

[98] Giordano, S. (2014) Explicit nonlinear homogenization for magneto-electro-elastic laminated materials. *Mechanics Research Communications*, **55** (0), 18–29.

[99] Mathur, N.D. (2008) The fourth circuit element. *Nature*, **455** (7217), E13–E13.